

Modeling and Testing Passive Daytime Radiative Cooling Devices

by
Genevieve DiBari

Professor Janice Hudgings, Advisor

A thesis submitted in partial fulfillment
of the requirements for the
Degree of Bachelor of Arts
in Physics

Pomona College
Claremont, California
May 3, 2023

Abstract

Passive Radiative Daytime Cooling (PRDC) is a phenomenon that permits a surface to cool below ambient temperatures when exposed to solar radiation without the input of an external power source. The goal of this project is to model, fabricate, and test novel PRDC devices. These devices work by emitting heat over a wavelength range in the infrared that is not absorbed by the atmosphere, enabling them to reach a lower temperature than the surrounding air. The devices are fabricated by depositing a thin layer of thermally evaporated silver that reflects radiation in the visible range onto a rigid substrate made of silicon or fused silica. The top layer is an outer coating of polydimethylsiloxane (PDMS), which emits radiation through the atmospheric window in the infrared. Under rooftop conditions, we have demonstrated that these devices can cool to 3-degrees Celsius temperature below ambient and to 20-degrees below control samples without PDMS.

Acknowledgments

I would first like to thank Professor Janice Hudgings. She has been a wonderful mentor and research advisor and I am deeply grateful for her unwavering guidance and support as I navigated college and this world of experimental research. I would also like to thank Paul McKinley who built this project up from nothing last year. Without his diligence and dedication to creating a strong foundation for this project, my work would not have been possible. Numerous people have also been an incredible help for this project along the way. Hardy Richardson helped me take my vague visions for what I wanted things to look like and made them a reality. I am very thankful for his talent and patience. Joseph Beardslee in the Chemistry Department helped me take the majority of my spectral measurements, which were a key component to the python model. Tag Curwen has also helped building the Stevenson Screen for the ambient probe.

I would also like to thank my family and friends for helping me get through college. My mom, Maria, and Sofia have been a wonderful support system for me; they have done a particularly good job tag teaming my calls these last 8 months. I also would like to thank Ana Mae Shickich for sharing half of a brain cell with me. Without her, I would not have made it through the physics major.

Contents

Abstract	i
Acknowledgments	ii
1 Introduction	1
1.1 Rise in Global Demand for Air Conditioning	1
1.2 Radiative Cooling	3
1.3 Previous Experiments and Current Applications	4
1.4 Previous Work On this Project and Project Goals	4
2 Theory	5
2.1 Passive Daytime Radiative Cooling Power	5
2.2 Electromagnetic Radiation	6
2.2.1 Conservation of Incident Radiation	7
2.2.2 Quantifying EM radiation	7
2.2.3 Transfer of Radiation	8
2.3 Solar Radiation	9
2.4 Blackbody Radiation	10
2.5 Atmospheric Transparency	11
2.5.1 Atmospheric Window	11
2.5.2 Variations in Transparency and Climate Variability	12
2.6 Earth's Radiative Energy Balance	13
2.6.1 Energy absorbed by the Earth's Surface	14
2.6.2 Energy Emitted by the Earth's Surface	15
2.6.3 Quantifying the Earth's Energy Balance	15
2.6.4 Radiative Forcing	17
2.7 Power Balance Equations	18
2.7.1 Power radiated from Device Surface	18
2.7.2 Radiation power density absorbed from the sun	19
2.7.3 Radiation power density absorbed from the atmosphere	20
2.7.4 Radiation power density absorbed from conduction and convection . .	20
2.8 Summary of Passive Daytime Radiative Cooling	21

3 Experimental Methods	22
3.1 Device Structures	22
3.2 Device Fabrication	22
3.3 Outdoor Rooftop Testing	24
3.4 Outdoor Set Up Robustness Testing	27
3.4.1 Device Fabrication	27
3.4.2 Measuring Ambient Temperature	29
3.5 Spectral Measurements	30
3.5.1 Procedure	30
3.5.2 Spectral Data	33
3.5.3 Summary	37
3.6 Specific Heat Capacity Measurements	38
3.6.1 Heat Capacity Results	40
3.6.2 Calculating change in device temperature	40
4 Experimental Results	42
4.1 Development of Power Balance Model	42
4.1.1 Power Radiated from the device: $P_{rad}(T_{dev})$	43
4.1.2 Power absorbed from solar radiation: $P_{sun}(\theta_{sun})$	45
4.1.3 Power absorbed from thermal radiation by the atmosphere: $P_{atm}(T_{amb})$	47
4.1.4 Power gained from conduction & convection: $P_{cond+conv}(T_{dev}, T_{amb})$	48
4.1.5 P_{cool}	48
4.1.6 Summary and limitations	49
4.2 Going from P_{cool} to device temperature	50
4.2.1 Extracting Steady State Temperature from P_{cool}	50
4.3 Comparing Device Performance	51
4.3.1 Silicon PDRC Device	52
4.3.2 Fused Silica PDRC Device	53
4.3.3 Summary of Model Results	53
4.4 Additional Model Tests	54
4.4.1 Adjusting Specific Heat	54
4.4.2 Adjusting Emissivity	55
4.4.3 Conclusions	55
5 Conclusions	56
5.0.1 Our Work	56
5.0.2 Future Directions	57
5.0.3 Final Remarks	58
A An appendix	59
A.1 Nicolet is50 FTIR Spectrometer Procedure	59
A.2 Data logger Manual	60

List of Figures

1.1	Predicted Global Stock of Air Conditioners. Millions of Air Conditioners is on the Y axis and years in on the X axis [26].	2
1.2	This is the atmospheric transmission window in which radiation is not absorbed by the atmosphere from 8 to 13 μm [13].	3
2.1	$P_{cond+conv}(T_{dev}, T_{amb})$, P_{sun} , $P_{atm}(T_{atm})$, are absorbed by the device and contribute to device heating. $P_{rad}(T_{dev})$ is radiated by the device and must outweigh the other three variables for the device to achieve a positive P_{cool} term and net cooling effect.	6
2.2	The main bands of the EM spectrum relevant to this discussion of the various radiative exchanges impacting PDRC devices are the visible and the infrared. [13]	6
2.3	The solid covers a larger area the further out one is from the emanating source [42].	8
2.4	The AM1.5 solar spectrum is a standard that depicts the amount of solar radiation that reaches the earth's surface. In this figure it is compared to the solar spectral irradiance striking the top of the earth's atmosphere [19]. . . .	9
2.5	Plot of blackbody curves at different temperatures [?].	10
2.6	Each atmospheric gas has a different absorption spectrum, giving rise to gaps in the atmosphere over which radiation is not absorbed [13].	12
2.7	This figure depicts the specific wavelengths at which each gas is transparent.	13
2.8	While the total solar irradiance incident on the earth is 1370 W/m^2 , only half of the earth receives solar radiation at a time [4].	14
2.9	Not all the incoming solar radiation is absorbed by the earth's surface. Some is absorbed by the atmosphere and earth. Some is reflected back into space [41].	15
2.10	Graph of the normalized blackbody curves for the sun and the earth from [33].	17
2.11	Radiative forcing is the difference between incoming radiation and outgoing radiation. If the earth is in equilibrium, it will maintain a constant temperature. Radiative forcing is a valuable parameter used to estimate how the global temperatures will rise in the future in response to changing concentrations of atmospheric gases and earth's albedo. [45]	18

3.1	Figure a) shows the cross-section of the Silicon (Si) based devices and figure b) shows the cross-section of the Fused Silica (FS) based devices	23
3.2	Graph of temperature probe calibrations.	26
3.3	Shows cross section of tested devices	27
3.4	Graph of rooftop experiment testing the structure of the fused silica device. .	28
3.5	Graph of rooftop experiment testing varying PDMS thicknesses.	28
3.6	Reference picture of a Stevenson Screen [39].	29
3.7	Picture of the Uv-Vis testing apparatus and 3D printed wafer stand.	31
3.8	Picture of the FTIR reflectivity testing setup with 10Spec.	32
3.9	Reflectivity and measured transmissivity spectra of bare Si wafer.	34
3.10	Absorptivity and emissivity spectra of bare Si wafer.	34
3.11	Measured reflectivity and transmissivity spectra of silver-coated silicon. . .	34
3.12	Absorptivity and emissivity spectrum of silver-coated silicon.	35
3.13	Measured reflectivity and transmissivity spectra of PDRC Si device.	35
3.14	Absorptivity and emissivity spectrum of PDRC Si device.	35
3.15	Measured reflectivity and transmissivity spectra of bare fused silica wafer substrate.	36
3.16	Absorptivity and emissivity spectrum of bare fused silica wafer substrate. .	36
3.17	Measured reflectivity and transmissivity spectra of fused silica wafer with Ag. .	36
3.18	Absorptivity and emissivity spectra of fused silica wafer with Ag.	37
3.19	Reflectivity and transmissivity spectra of fused silica PDRC device.	37
3.20	Absorptivity and emissivity spectra of fused silica PDRC device.	37
3.21	Picture of the Al block, Peltier Cooler, device, and Styrofoam setup.	39
4.1	Blackbody Spectrum from power balance model relative to reference plot [18].	43
4.2	Black Body Spectrum at lower temperatures.	44
4.3	Graph of $P_{rad}(T_{dev})$ versus device temperature for the silicon PDRC devices and bare silicon wafer. As temperature falls, so does the rate at which the device converts thermal energy to outgoing radiation.	44
4.4	Graph of the log base 10 of $P_{rad}(T_{dev})$ and T_{dev}	45
4.5	Graph of $P_{sun}(\theta_{sun})$ versus device temperature T_{dev} for the silicon PDRC device and bare silicon measured at normal incidence ($\theta_{sun} = 0$). Note there is no temperature dependence.	46
4.6	The AM1.5 spectrum used in the power balance model extracted from NREL open-source terrestrial solar spectral irradiance data [36].	46
4.7	This graph shows the relationship between $P_{atm}(T_{amb})$ and ambient temperature for the silicon PDRC device and bare silicon.	47
4.8	Graph of $P_{cond+conv}(T_{dev}, T_{amb})$ against the difference between T_{dev} and T_{amb} for the silicon PDRC device and bare silicon wafer.	48
4.9	Graph of P_{cool} against device temperature for silicon PDRC device and bare silicon. P_{cool} becomes negative at $T_{dev}=302.5$ K for the PDRC silicon device and at $T_{dev}=318.8$ K for the bare silicon.	49

4.10 Graph of $\Delta T_{device}/\text{second}$ against P_{cool} for the Silicon PDRC device. T_{amb} is assumed to be 307K.	51
4.11 Graph of T_{device} against time for the silicon PDRC device and bare silicon wafer	51

Chapter 1

Introduction

This work focuses on building, modeling, and testing Passive Daytime Radiative Cooling (PDRD) devices. Rather than heating up as typical surfaces do, these layered structures lower their temperature when in the presence of solar radiation without the need of electricity. As a result, passive daytime radiative cooling technology is seen as a possible solution to the global cooling crisis this world will face as temperature rises above the level suitable for healthy living environments.

1.1 Rise in Global Demand for Air Conditioning

Air conditioning is quickly becoming a necessity. It is an unequivocal fact that global temperatures are on the rise and as heat waves become more extreme and frequent, the world will grow more reliant on air conditioning. Only 8 percent of the population living in the hottest environments own an air conditioning unit according to a study published by the International Energy Agency (IEA) in 2020 [26]. Yet, air conditioning sales will rise, especially in newly developing economies. The global energy demand for air conditioning is expected to triple by 2050 [26]. To meet this rise in demand, the stock of air conditioners in buildings would need to rise from 1.6 billion in 2018 to 5.6 billion in 2050, equivalent to 10 AC units sold every second over the next 30 years as shown in figure 1.1 [26]. Air conditioning will become one of the main drivers of electricity demand over these next 30 years [30]. Already 10 percent of global electricity consumption is due to air conditioning [26].

There are three main concerns with these systems. Firstly, conventional compressed air conditioning units rely on a liquid refrigerant, typically hydrofluorocarbons (HFCs), to expand and compress as the liquid transfers heat from one place to other. These HFCs are estimated to be 2000 times more potent greenhouse gases than CO_2 [37]. Leakages will become increasingly prevalent as usage of these units rise, particularly in rapidly growing economies like China, India, and Indonesia [26]. Second, these systems do not eliminate heat, rather they displace it by expelling the heat to surrounding air. As a result, conventional units contribute to urban heat islands [20]. Lastly, these units are energy intensive. Currently, as a global average, 20 percent of building electricity usage is devoted to air

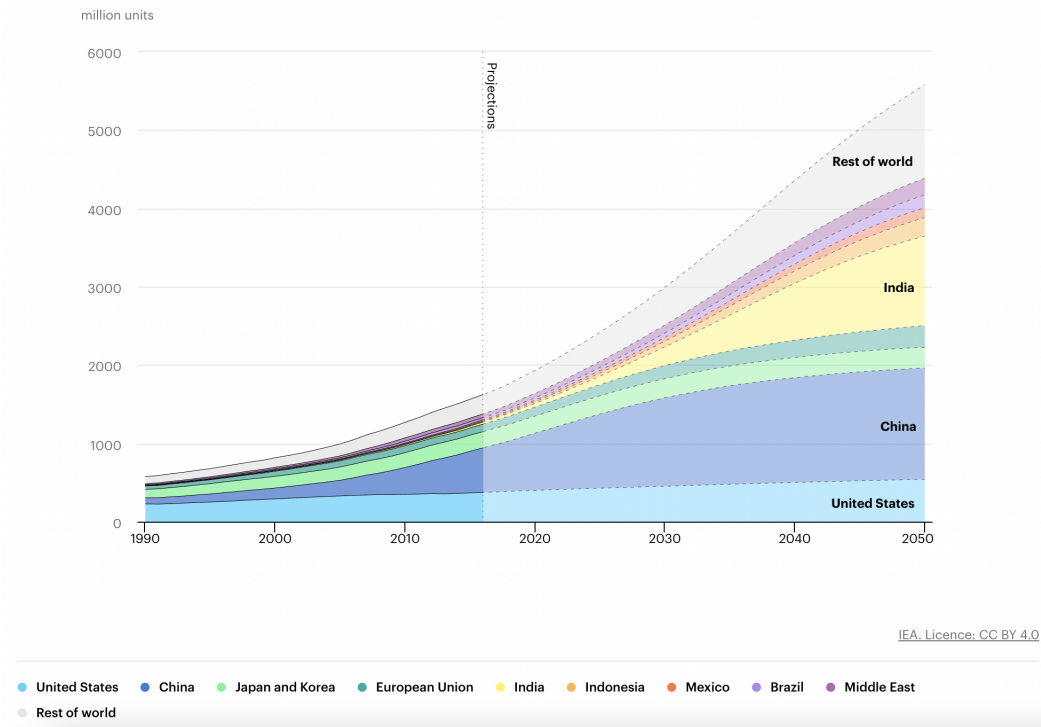


Figure 1.1: Predicted Global Stock of Air Conditioners. Millions of Air Conditioners is on the Y axis and years in on the X axis [26].

conditioning and fans[20]. As a result, these units increase the demand for electricity.

As extreme weather events increase, heat waves and the global demand for electricity will place higher strain on the electrical grid, making the grid more vulnerable to outages. In California, for instance, during heat waves air conditioning has accounted for 60 to 70 percent of electricity demand [3]. System operators must meet electricity demand on a moment-to-moment basis. Therefore, when demand exceeds the supply of electricity, it can lead to power outages, placing people and communities at risk for heat related health complications. Furthermore, during these periods of higher demand, electrical grid operators ramp up easily dispatchable power plants to meet the rise in demand. These power plants are more expensive to operate and are typically natural gas or combined heat and power plants, which are non-renewable, carbon emitting electricity generation sources.¹ As the electrical grid supplies more power, those additional incremental units of generation release more carbon emissions into the air.

Currently, air conditioning units are estimated to contribute to 3.94 percent of global greenhouse gas emissions [37]. However, as demand increases, this percentage is also expected to rise. By 2100, the world economic forum estimates that emissions from air conditioning units are projected to account for a 0.5 degree Celsius global temperature rise [34].

¹Hydroelectric plants are one of the few renewable energy sources that have a high ramping capability.

More efficient air conditioning units can help drive down the peak demand for electricity, which in turn lowers emissions and costs. While energy efficiency of the average HVAC unit has improved by 50% since the 1990s, the energy efficiency ratio of the average units sold is still half of the most efficient technology available [26]. Upfront costs are the main barrier, especially in emerging economies. Therefore, efforts to improve cooling efficiency must also consider the relative costs of the available cooling technologies.

1.2 Radiative Cooling

Hot objects emit energy in the form of photons, also known as black body radiation. Radiative passive cooling refers to when objects naturally lower their temperatures beyond the temperature of the surrounding air by emitting more blackbody radiation than they absorb from the sun and other surfaces. If the surfaces' blackbody radiation is emitted over the wavelengths not absorbed by the atmosphere, the object can exchange heat with the essentially infinite cold reservoir of deep space [46]. This atmospheric window, over which radiation is not absorbed, is from 8 to 13 μm as shown in figure 1.2. This phenomenon, known as Passive Radiative Cooling, can occur naturally. For instance, frost can form on nights when temperatures do not reach below freezing, because the outgoing radiation exceeds incoming radiation, allowing the ground to be colder than the ambient air [10].

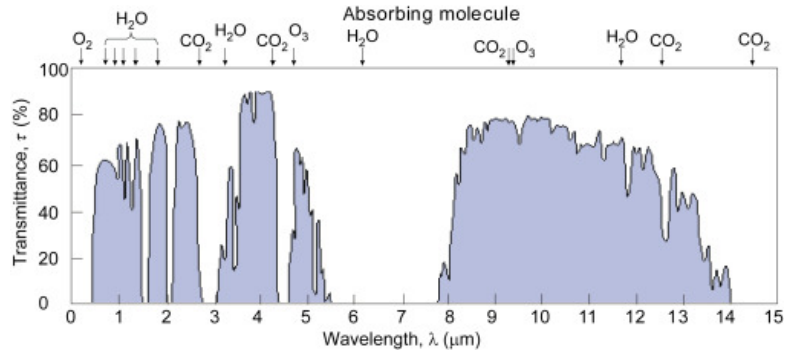


Figure 1.2: This is the atmospheric transmission window in which radiation is not absorbed by the atmosphere from 8 to 13 μm [13].

While frost can achieve sub-ambient cooling at night, to achieve sub-ambient cooling during the day, surfaces need to be highly reflective in the visible range in addition to being emissive over the atmospheric window. Snow is example of a passive daytime radiative cooler. Snow utilizes this cooling phenomena during the day by being highly reflective in the visible range, in addition to being highly emissive over long wave radiation (0.2 μm - 4 μm) [46]. Snow's highly reflective surface reflects back the portion of the sun's short wave thermal radiation, which limits the snow's thermal absorption [25].

Devices designed for passive daytime radiative cooling (PDRC), known as thermal emitters, mimic the properties of snow, by being highly reflective in the visible range, and highly emissive in the IR range over the main atmospheric transmission window [46].

1.3 Previous Experiments and Current Applications

The idea of utilizing PDRC arose in the late 1960s with Trombe, followed by the first experimental work in 1975 with S. Catalanotti et al; however, this first experiment was only successful under nighttime conditions [44][14]. Recent experimental work has achieved significantly higher levels of sub-ambient cooling. These experiments have measured cooling performances ranging from 2°C to 15°C[15].

There are two main approaches to building PDRC devices [47][12][46][49][40][32][23]. The first approach uses multi-layered nanostructures that utilize the various radiative properties of different materials. Raman et al. used this approach and constructed multi-layers of dielectric films consisting of hafnium dioxide (HfO_2) and silicon dioxide (SiO_2) that demonstrated daytime cooling of 4.9°C [40]. Kou et al. coated fused silica substrates with highly reflective silver and emissive polydimethylsiloxane (PDMS) to achieve 8.2°C of cooling in daytime conditions and 8.4°C under nighttime conditions [27]. Zhou et al. used layered thermal emitters coating aluminum substrates with a 150 μm of PDMS to achieve 2-9°C cooling effect during daytime testing [49]. Gentle and Smith utilized the second approach, which involved mixing materials with varying refractive indices to achieve high reflectivity over the solar wavelengths. Gentle and Smith used a mixture of crystalline Silicon carbide (SiC) nanoparticles and silicon dioxide (SiO_2) for a sub-ambient daytime cooling performance of 12-17°C depending on the climate [23].

Passive Daytime Radiative Cooling devices offer numerous applications as electricity free coolers. In buildings, cooling systems, which include AC, fans and refrigerators, account for 20% of electricity usage [26]. Therefore, PDRC technologies can be incorporated into building design to improve overall cooling efficiency. A company based out of Stanford University, SkyCool Systems, integrated PDRC devices into air conditioning and refrigeration systems to increase their energy efficiency by up to 40 percent [2]. PDRC technologies can be used in roofing and side paneling materials. For instance, Li et al. developed a radiative cooling wood [31]. Mandal et al proved that passive cooling technologies can also be implemented in paints [35].

1.4 Previous Work On this Project and Project Goals

This thesis will build off the progress made by Paul McKinley Class of 2022. McKinley began the PDRC project in Fall of 2021 in Professor Hudging's lab as his senior thesis project. He laid the groundwork for my thesis by developing the fabrication process for the PDRC devices detailed in my methods chapter. He also successfully demonstrated a 3°C sub-ambient cooling with his outdoor testing setup and a 20°C cooling with the control wafer. His outdoor testing results are described in more detail in the results section.

My contribution to this project focuses on modeling PDRC devices in python while also improving upon the initial outdoor testing setup. My goal for this model is to predict sub-ambient temperature changes for the PDRC devices that match what we would realistically see in our outdoor testing setup.

Chapter 2

Theory

At the most general level, Passive Daytime Radiative Cooling devices reach sub-ambient cooling, a temperature lower than that of the surrounding air, when the amount of blackbody radiation they emit exceeds the thermal radiation they absorb. PDRC devices are able to achieve this result in the presence of solar radiation because they are highly reflective over the solar spectrum and highly emissive in the IR, over a wavelength window in the atmosphere that minimally absorbs thermal radiation. This chapter develops a detailed model of the radiative exchanges between the earth, the atmosphere, the sun, and the passive daytime radiative cooling devices that permit this result to occur.

2.1 Passive Daytime Radiative Cooling Power

Heat is transferred from the passive daytime radiative coolers through thermal emission. The amount of power that these devices emit is referred to as $P_{rad}(T_{dev})$, where T_{dev} is the temperature of the PDRC device. The surrounding environment contains various sources of heating that limit the device's cooling capacity: the power absorbed from the sun P_{sun} , the thermal radiative power emitted by the warm atmosphere and then absorbed by the device $P_{atm}(T_{amb})$ at ambient temperature T_{amb} , and the heat transfer from conduction and convection $P_{cond+conv}(T_{dev}, T_{amb})$.

The overall cooling capacity of the PDRC devices is determined by the relative magnitude of these sources. When $P_{rad}(T_{dev})$ exceeds the sum of P_{sun} , $P_{atm}(T_{amb})$, and $P_{cond+conv}(T_{dev}, T_{amb})$, cooling is achieved. This relation is shown in Equation 2.1 and in Figure 2.1.

$$P_{cool} = P_{rad}(T_{dev}) - P_{atm}(T_{amb}) - P_{sun} - P_{cond+conv}(T_{dev}, T_{amb}) \quad (2.1)$$

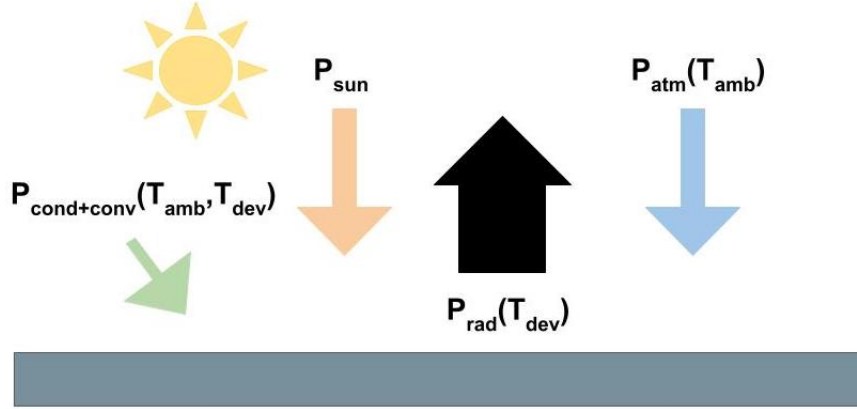


Figure 2.1: $P_{\text{cond+conv}}(T_{\text{dev}}, T_{\text{amb}})$, P_{sun} , $P_{\text{atm}}(T_{\text{atm}})$, are absorbed by the device and contribute to device heating. $P_{\text{rad}}(T_{\text{dev}})$ is radiated by the device and must outweigh the other three variables for the device to achieve a positive P_{cool} term and net cooling effect.

2.2 Electromagnetic Radiation

Solar Radiation and blackbody radiation are the primary ways in which heat is transferred in and out of the earth's system. Both are forms of electromagnetic radiation albeit over different wavelength ranges, as shown in Figure 2.2.

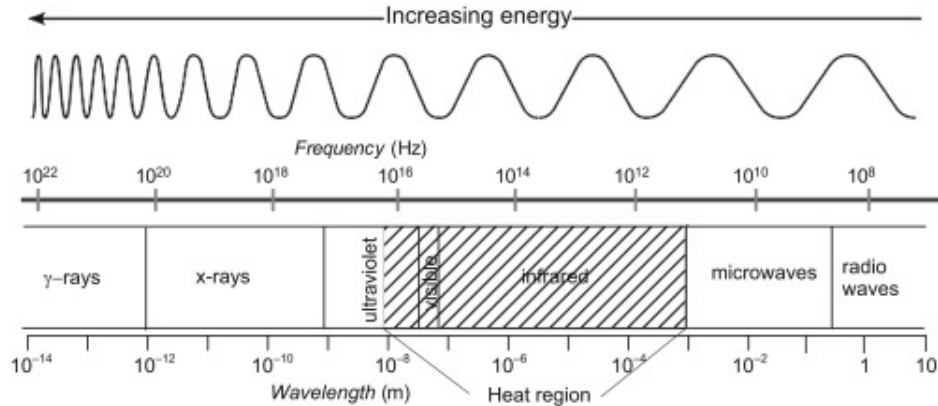


Figure 2.2: The main bands of the EM spectrum relevant to this discussion of the various radiative exchanges impacting PDRC devices are the visible and the infrared. [13]

Materials have wavelength dependent ability to absorb, reflect, and transmit EM radiation [13]. As displayed, all around us, colors result from surfaces absorbing certain wavelengths of light and reflecting others. Yet, their reflectivity trails off at longer wavelengths. This wavelength variation in reflectivity is largely dependent on how λ compares to the surface's molecule size [24]. A surface with small molecule surface composition will be more reflective of long wave radiation because the radiation sees the surface as homogeneous and

smooth [24]. Given this wavelength dependence of reflectance, an object or surface could be highly reflective at some wavelength ranges, but not others. Passive Daytime Radiative Coolers are highly reflective in the visible range due to their silver coating. Similarly, the atmosphere is transparent at some wavelengths and highly reflective or absorbent at others.

2.2.1 Conservation of Incident Radiation

Given that EM radiation carries energy, it is subject to conservation laws. The first conservation law, Equation 2.2, tells us that of the radiation incident upon a surface, the fraction of radiation reflected $\rho(\lambda)$ (reflectivity), transmitted $\tau(\lambda)$ (transmissivity), and absorbed $\alpha(\lambda)$ (absorptivity) by a surface must equal one [13].

$$\rho(\lambda) + \tau(\lambda) + \alpha(\lambda) = 1 \quad (2.2)$$

2.2.2 Quantifying EM radiation

Flux density and intensity both measure the strength of EM radiation. Understanding the difference between flux and intensity is valuable for recognizing where each of the components in Equation 2.1 are derived from. All definitions for flux density, flux, intensity, etc come from Grant W Petty's "A First Course in Atmospheric Radiation" [24].

Flux Density

Radiant power density is a measure of either the radiation emitted by a given object or the amount of radiation incident on a given surface.¹ This value, also known as flux density, Φ , is determined by the number of photons passing through a given area and has units $\frac{W}{m^2}$. Irradiance is another term used to describe the same quantity as flux density and is often used to describe radiation incident on a surface. Exitance is used to describe radiation emitted from a surface.

$$\Phi = \frac{\text{number of photons}}{(\text{unit area})} \quad (2.3)$$

Flux density for an extended wavelength range considers the number of photons emitted in a small wavelength interval around a specific wavelength of light [5].² Therefore, units for broadband flux density, also referred to as spectral irradiance, are $\frac{W}{(m^2)(m)}$.

Intensity

Intensity is a measure of both strength and direction of the incident flux on a surface. Intensity and incident flux are closely related. As a cloud passes over head, the intensity of

¹Flux is often used as shorthand for flux density. However, technically flux only has the units watts W. For this thesis, I will use flux density.

²Broadband radiation is radiation that comprises a range of wavelengths. Solar radiation is broadband.

radiation from that direction falls, causing the incident flux and overall available radiation on the earth's surface to fall. With this in mind, intensity is the flux density, measured normal to the beam per unit solid angle traveling in a certain direction $\hat{\Omega}$ [24]. It is the power per unit area per unit solid angle [24]. Hence, while flux density could be thought of as the total brightness of a source per unit area, intensity measures the brightness at a particular point.

As radiation moves further away from the source, the radiation is spread over a larger area, so the intensity decreases. Hence, the rays weaken. Intensity is, therefore, dependent on the distance an object is from the emitting source. This distance calculation is captured using the solid angle, $d\Omega$. The solid angle can be thought of as a measure of the field of view from a particular point.³ The solid covers a larger area the further out one is from the source [11]. Units of intensity are $\frac{W}{m^2 SR}$, where SR represents a steradian, which is a unit-less measure of the solid angle. Figure 2.3 is a visual depiction of a solid angle.

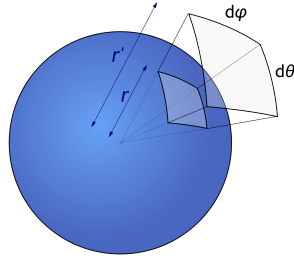


Figure 2.3: The solid covers a larger area the further out one is from the emanating source [42].

In order to calculate the incident flux on a surface, one has to integrate the intensity from all possible directions $d\Omega$ visible from the surface.

2.2.3 Transfer of Radiation

Thermal emission is the process by which "the internal energy of a material is converted into radiant energy" [24]. Thermal emission is the mechanism by which heat is exchanged between space, the atmosphere, and the earth's surface. Without this form of radiation, the earth would indefinitely heat up due to the incoming solar radiation [24]. Furthermore, the downwards thermal emission from the atmosphere and clouds keeps the earth warm at night. Dryer climates experience more extreme temperature drops at night due to the lower capacity of the atmosphere to absorb radiation. Thermal emission is energy that is radiated in the form of discrete photons and is determined by the object's absolute temperature and material composition [13].⁴

³A useful analogy from the Grant W Petty's "A First Course in Atmospheric Radiation": a solid angle is to 'regular' angle as area is to length [24].

⁴Ten% of absorbed solar energy is radiated directly out to space, which is 6% of the total energy absorbed from the sun. The remaining 90% of absorbed energy is eventually released into space by being transferred to

2.3 Solar Radiation

Solar radiation is electromagnetic radiation emitted from the sun. The solar spectrum AMI1.5 in Figure 2.4 depicts the solar irradiance or incident flux emitted by the sun that reaches the earth at sea level, after being transmitted through the earth's atmosphere. The incident flux received by the earth's surface depends on the distance between the sun and Earth, the angle θ_{sun} at which the sun's rays hit the atmosphere and surface, the atmospheric gases and contaminants in the air, as well as weather [19]. These last two factors contribute to the difference in incident flux at the top of the atmosphere and on the earth's surface as seen in Figure 2.4.

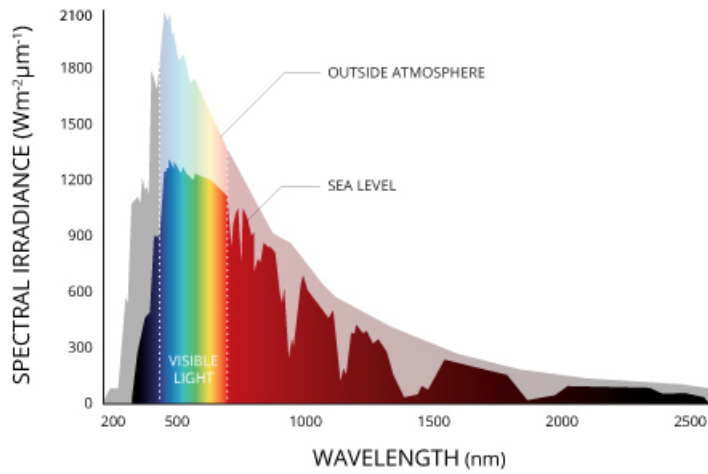


Figure 2.4: The AM1.5 solar spectrum is a standard that depicts the amount of solar radiation that reaches the earth's surface. In this figure it is compared to the solar spectral irradiance striking the top of the earth's atmosphere [19].

The incident flux from the sun extends over the wavelengths from ultraviolet to infrared light SP. Of the energy radiated from the sun, 99% is within $0.1\mu\text{m}$ and $4\mu\text{m}$; most solar radiation is split between the visible band and the near infrared band [24]. Given the wavelength dependence of light, shorter wavelengths carry more energy. Therefore, it follows that the visible range contains the maximum radiation emitted by the sun; almost half of the total power output from the sun is within the visible band [24]. PDRC devices are intentionally designed to be highly reflective of solar radiation over the visible range to limit absorption of these higher energy photons. By reflecting these wavelengths, PDRC devices minimize absorbed solar radiation, and therefore, limit their heating due to the sun.

the atmosphere through evaporation of surface moisture, thermal conduction, and re-absorption of emission [24]. The atmosphere is the main actor in radiating this energy back into space.

2.4 Blackbody Radiation

The energy transfers described in Figure 2.1 rely on an important phenomenon of all objects with non-zero temperature, blackbody radiation. Every object with a non-zero temperature emits energy because of the object's electrons [13]. Plank's Function, Equation 2.4, describes blackbody radiation per unit area per unit wavelength. Units of blackbody radiation are $\frac{W}{m^3 SR}$ because it is a measure of intensity.⁵

$$Ibb_\lambda(T, \lambda) = \frac{2hc^2}{\lambda^5(e^{\frac{hc}{\lambda k_B T}} - 1)} \quad (2.4)$$

Blackbody surfaces that have an emissivity (ϵ) of one have a higher measure of intensity relative to surfaces that are not blackbodies. A grey body refers to a surface that only absorbs and emits some of the radiation that it receives. Note an object's emissivity refers to the fraction of radiant energy emitted by a surface relative to the radiant energy of a blackbody at the same temperature [24]. Figure 2.5 shows Planck's function for blackbody radiation calculated at various temperatures. Notice that as temperatures falls, so does peak blackbody intensity.

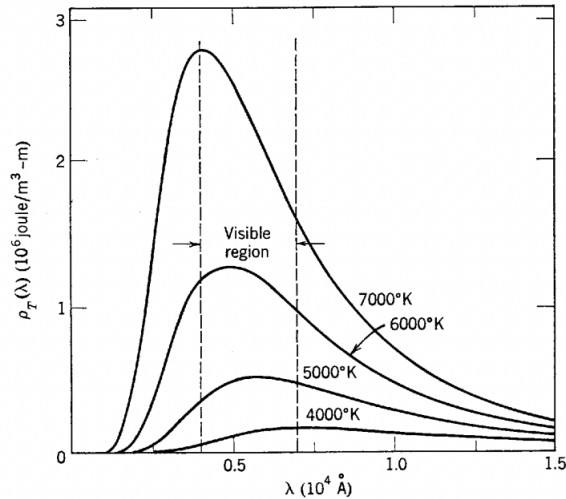


Figure 2.5: Plot of blackbody curves at different temperatures [?].

Plank's function describes radiation for monochromatic light because it is calculated over wavelength intervals $\lambda + \delta\lambda$ [24]. Stefan's Boltzmann Law integrates over all wavelengths and the solid angle of one hemisphere to describe the flux density for broadband radiation from a blackbody.⁶

⁵The speed of light (c): 2.998, Planck's constant (h): $6.626 \times 10^{-34} \text{ Js}$, Boltzmann's constant (k_B) : $1.381 \times 10^{-23} \text{ J/K}$.

⁶The integral of the solid angle of one hemisphere comes out to π [24].

$$R_{BR}(T) = \pi \int_0^{\infty} B_{\lambda}(T) d\lambda = \sigma T^4 \quad (2.5)$$

This relation means that a surface radiates energy at a value that is proportional to the fourth of its temperature scaled by the Stefan-Boltzmann constant ($\sigma = 5.6710^8 W/m^2 K^4$). PDRC devices emit blackbody radiation to lower their temperature. These devices are tailored specifically to emit their radiation at wavelengths that the atmosphere does not absorb. By doing so, PDRC devices transfer their heat into space rather than the atmosphere. Further discussion for how this is achieved is in the following section.

For an object in thermal equilibrium, Kirchhoff's Law of energy conservation, Equation 2.6, states that absorptivity $\alpha(\lambda)$ at each wavelength equals its emissivity $\varepsilon(\lambda)$.

$$\alpha(\lambda) = \varepsilon(\lambda) \quad (2.6)$$

An object could be a poor emitter at short wavelengths, while strong at longer wavelengths. For instance, fused silica has a high transmissivity and low absorptivity in the visible range. Yet, it has high emissivity in the IR. An object that absorbs all the radiation that is incident on its surface is a blackbody [24].

2.5 Atmospheric Transparency

Atmospheric gases govern the wavelengths at which radiation is mainly absorbed, reflected, or transmitted out into space. The atmosphere is made up of 78% nitrogen, 21% oxygen, and .93% argon. Trace gases, such as carbon dioxide CO_2 , ozone CO_3 , methane CH_4 , and nitrous oxide N_2O make up the remaining percentage [29]. Water vapor, H_2O , is an additional constituent in the atmosphere. However, the concentration of H_2O in the atmosphere depends dramatically on climate and weather patterns [29].

2.5.1 Atmospheric Window

Each of these gases absorb radiation at different wavelengths. As depicted in Figure 2.6, in the thermal IR band (from 4m to 50m), CO_2 , O_2 , CO_3 , and H_2O are the main gases driving atmospheric transparency [24].⁷ Hence in areas with dryer climates, the atmosphere may be significantly more transparent. Other effects such as scattering from aerosols impact transmission in the visible range, however these effects are minimal at the longer wavelengths [13].

Overlaying these absorption bands give rise to wavelength regions over which the atmosphere is largely opaque to radiation and regions over which the atmosphere is transparent. These transparency regions are referred to as atmospheric windows. Radiation emitted from earth within these windows escapes directly into space and therefore does not contribute

⁷Carbon dioxide absorbs IR radiation at around 4.3m and more strongly at 15m. Water vapor absorbs IR radiation beginning at 6.3m and at points between 0.7m and 3 m [13].

to atmospheric warming [24]. The main window that this project focuses on is in the IR, from 8m and 13m. Very few atmospheric gases absorb radiation in this region with the main active agent in this region being H_2O . This means that the more humid the environment, the more opaque this window becomes.⁸

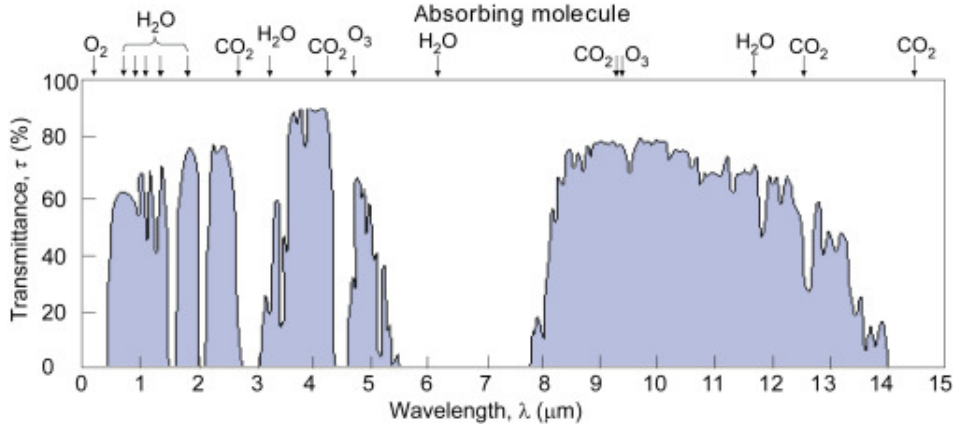


Figure 2.6: Each atmospheric gas has a different absorption spectrum, giving rise to gaps in the atmosphere over which radiation is not absorbed [13].

2.5.2 Variations in Transparency and Climate Variability

Variations in these atmospheric gases have profound impacts on climate variability ???. Industrialization of the modern economy in the last 150 years has caused a rapid increase in CO_2 , impacting overall atmospheric transparency and thus atmospheric heating. CO_2 is a significant greenhouse gas; yet it is not the only atmospheric gas that absorbs radiation and traps heat in our atmosphere. Water vapor, H_2O , is the largest greenhouse gas by concentration. As the temperature increases, the atmosphere's ability to retain moisture rises, contributing further to atmospheric heating. Other greenhouse gases include CH_4 , which is 30 times stronger than CO_2 , ozone O_3 , and nitrous oxide N_2O [9].

Similarly, to CO_2 , human activity has driven increases in other greenhouse gas concentrations in the atmosphere. Currently, methane emissions are responsible for 30% of the global rise in temperatures according to the IEA and these global emissions are expected to rise [7]. Methane CH_4 , which is released from decomposing organic materials, has seen this recent rise due to agriculture. In particular, livestock manure and gastroenteric emissions have accounted for more than a third of human caused CH_4 emissions [7]. Furthermore, when CH_4 enters the atmosphere, it interacts with carbon monoxide and nitrous oxides to form ozone O_3 . The ozone layer in the stratosphere is highly absorbent of UV light and therefore, prevents damaging rays from reaching the earth's surface. However, tropospheric ozone that forms from CH_4 emissions is a toxic air pollutant and greenhouse gas [16]. As

⁸There exists other windows in almost every spectral band, such as a window between 80GHz and 100GHz, which is incredibly important for satellite imaging [24].

the concentration of these greenhouse gases in the atmosphere rises, so does the capacity of the atmosphere to retain thermal energy.

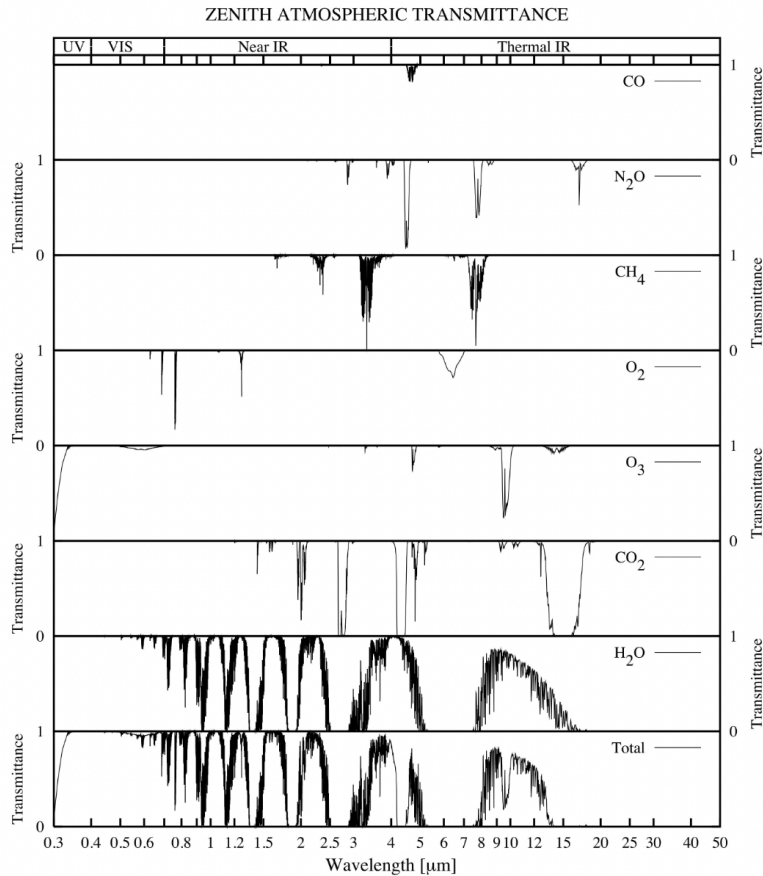


Figure 2.7: This figure depicts the specific wavelengths at which each gas is transparent.

2.6 Earth's Radiative Energy Balance

For the earth to maintain a constant temperature, the amount of incoming radiation must balance with the amount of outgoing radiation. Therefore, the magnitude of the solar radiation absorbed must be equal to the amount emitted.

$$E_{absorbed} = E_{emitted} \quad (2.7)$$

Solving for these two values can reveal the equilibrium temperature at which the earth is in an energy balance with the incoming solar radiation.

2.6.1 Energy absorbed by the Earth's Surface

The total solar irradiance on the earth is S_o 1370 W/m^2 .⁹ Accounting for the curvature of the earth and the fact that only half of the earth receives solar radiation at a time, the global average value of the incident flux at the top of the earth's atmosphere is 342 W/m^2 [4].

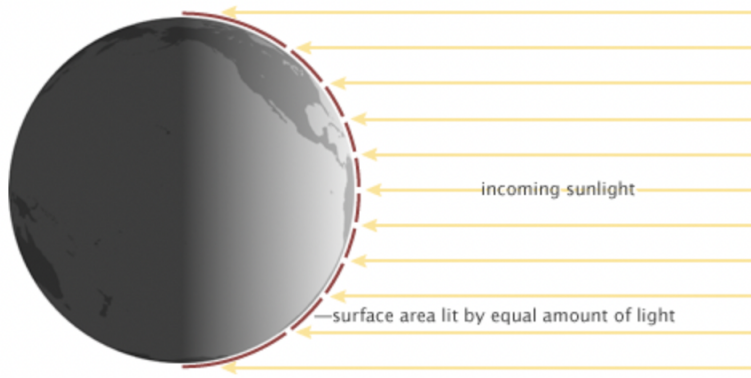


Figure 2.8: While the total solar irradiance incident on the earth is 1370 W/m^2 , only half of the earth receives solar radiation at a time [4].

Of the radiation that collides with the earth's upper atmosphere, not all of it will be absorbed by the earth's surface due to the albedo of the earth. The albedo of the earth refers to the overall percentage of light that is reflected by a surface. Due to clouds, the atmosphere, and reflective materials like ice and snow, about 30% of the incoming solar radiation is reflected into space. Only 51% of the incoming solar radiation is absorbed by the land and oceans. The remaining 19% is absorbed by the atmosphere and clouds. Figure 2.9 illustrates the balance between the incoming solar radiation and the outgoing radiation from the earth and atmosphere.

Since albedo represents the percentage of light reflected, the amount of incoming solar radiation absorbed by the earth's surface is proportional to one minus the earth's albedo. Therefore, the total solar radiation absorbed by the earth's surface equals roughly:

$$\frac{(1370 \text{ W/m}^2)}{4}(1 - 0.3) = 239 \text{ W/m}^2 \quad (2.8)$$

A more quantitative equation for $E_{absorbed}$ is as follows:

$$E_{absorbed} = S_o * (1 - A) * \pi R_E^2 \quad (2.9)$$

S_o represents the total solar irradiance, A is the albedo of the earth, calculated to be roughly .30 on average, and πR_E^2 represents the cross-sectional surface area of the earth. A full calculation of the amount of radiation absorbed by the earth's surface using equation 2.9 is in section 2.6.3.

⁹Geographic location, climate, cloud cover, time of day, and season are all factors that impact the amount of solar radiation that reaches the earth's surface [17].

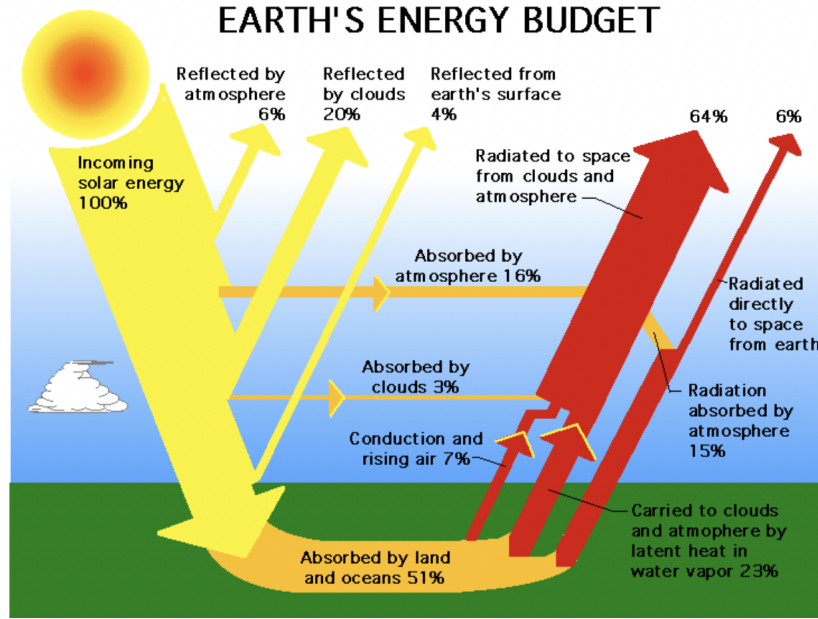


Figure 2.9: Not all the incoming solar radiation is absorbed by the earth's surface. Some is absorbed by the atmosphere and earth. Some is reflected back into space [41].

2.6.2 Energy Emitted by the Earth's Surface

The radiation emitted by the earth's surface $E_{emitted}$ can be calculated using Equation 2.5. By this law, the earth emits radiation proportional to the fourth power of its temperature multiplied by the surface area over which it emits [?].

$$\begin{aligned} E_{emitted} &= I_{bb}(T_E) * \text{Surface Area} \\ &= \sigma T_E^4 (4\pi R_E^2) \end{aligned} \quad (2.10)$$

I_{bb} represents the blackbody spectrum at the temperature of the earth T_E . The R_E^2 term, which equals $6.378 * 10^6$, is the radius of the earth. Finally, $\sigma = 5.67 * 10^{-8} W/m^2 K^4$ is the Stefan-Boltzmann constant.

2.6.3 Quantifying the Earth's Energy Balance

As mentioned above, in order for the earth to maintain a constant temperature, the amount of solar radiation absorbed must equal the amount of blackbody radiation emitted by the earth. Approximating the surface area of the earth modeled as a sphere, we can estimate the temperature at which the earth resides in order to maintain this radiative balance. The blackbody temperature of the earth can be calculated by setting equation 2.9 equal to equation 2.10.

$$E_{absorbed} = E_{emitted} \quad (2.11)$$

$$\begin{aligned} S_o * (1 - A) * \pi R_E^2 &= \sigma T^4 (4\pi R_E^2) \\ S_o * (1 - A) * \left(\frac{1}{4}\right) &= \sigma T^4 \end{aligned} \quad (2.12)$$

Note that plugging in the variables on the left yields the same result as Section 2.6.1 for incident flux on the earth's surface.

$$\begin{aligned} 1370W/m^2 * (1 - .3) * \frac{1}{4} &= \sigma T^4 \\ 239W/m^2 &= \sigma T^4 \end{aligned} \quad (2.13)$$

The blackbody temperature of the earth can be calculated by rearranging equation 2.12.

$$\begin{aligned} S_o * (1 - A) * \pi R_E^2 &= \sigma T^4 (4\pi R_E^2) \\ T &= \sqrt[4]{\frac{S_o(1 - A)(\frac{1}{4})}{\sigma}} \\ T &= \sqrt[4]{\frac{239W/m^2}{5.6704 * 10^{-8}W/m^2K^4}} \\ T &= 255K \end{aligned} \quad (2.14)$$

Converting from Kelvin to Celsius

$$T = 255K - 273K = -18C \quad (2.15)$$

Figure 2.10 shows the normalized blackbody curves of the sun and the earth [33].¹⁰ These graphs show the earth's blackbody radiation peaks in mid-IR wavelength region, reaching an equilibrium surface temperature of 255 K (-18 °C), consistent with the above calculation. However, the average global temperature is 14°C, while the blackbody temperature calculated above is -18°C [6]. What the above calculation fails to involve are the atmospheric gases which absorb and re-emit radiation, trapping the heat that maintains the earth at a temperature suitable for life.

¹⁰the normalized graph is so that the area's under each curve are equal

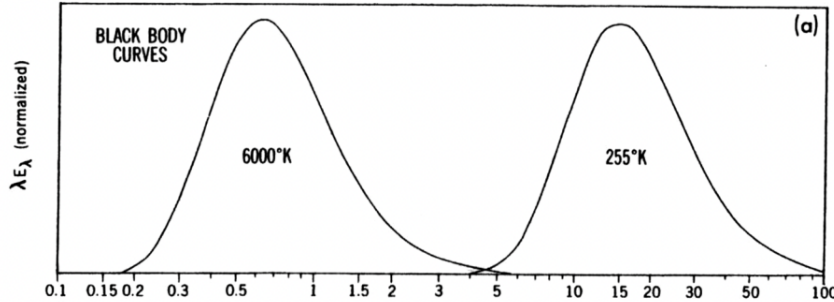


Figure 2.10: Graph of the normalized blackbody curves for the sun and the earth from [33].

2.6.4 Radiative Forcing

Radiative forcing, in this case, is a measure of how the balance of incoming and outgoing radiation is impacted by changing ppm of a particular gas [45]. As these gases in Figure 2.7 such as CO_2 and CH_4 increase in concentration in the atmosphere, their radiative forcing rises. Just like any object with a non-zero temperature, the earth emits blackbody radiation. The blackbody temperature of the earth calculated in equation 2.13 is roughly 32°C below the average temperature of the earth. As these greenhouse gasses' concentrations in ppm increases in the atmosphere, their ability to drive the earth further from its blackbody temperature grows. Figure 2.11 shows radiative forcing values relative to the baseline year 1750 prior to the industrial revolution in the united states.

Passive daytime radiative cooling devices work to help limit the radiative forcing caused by human activity. Radiation that is absorbed by the device is re-emitted within the atmospheric window, between 8 μm and 13 μm , such that the radiation escapes into space rather than absorbed by these gases. As an electricity free alternative to air conditioning, PDRC devices also reduce the overall energy demand and thus carbon emissions caused by the rising need for cooling.

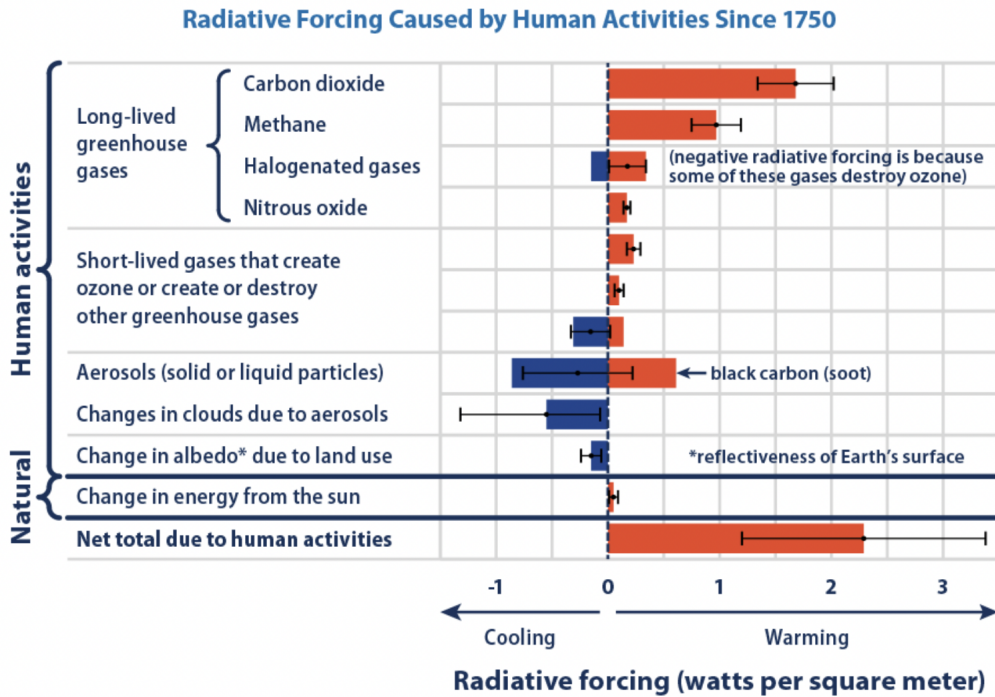


Figure 2.11: Radiative forcing is the difference between incoming radiation and outgoing radiation. If the earth is in equilibrium, it will maintain a constant temperature. Radiative forcing is a valuable parameter used to estimate how the global temperatures will rise in the future in response to changing concentrations of atmospheric gases and earth's albedo. [45]

2.7 Power Balance Equations

Understanding the different atmospheric variables that impact the exchange of radiation amongst the sun, earth's surface, and atmosphere is important for understanding passive daytime radiative cooling. These exchanges allow the devices to lower their temperature below ambient in the presence of solar radiation.

It is important to note that the following equations output power by multiplying the calculated flux density by the unit area of the devices. Hence the units of all the below equations are watts ($W/m^2 \cdot m^2 = W$). In order to calculate the flux incident on a surface, these equations break down further to look at the intensity for each solid angle and then integrates over all solid angles to calculate the flux density. Given intensity is measured normal to the beam, when integrating over all solid angles, the equations for the various flux densities pick up a $\cos(\theta)$ term.

2.7.1 Power radiated from Device Surface

As mentioned earlier in the section, every object with a non-zero temperature emits a certain amount of radiation that is tied to its temperature. The radiated power of the device,

$P_{rad}(T_{dev})$, calculates the “radiation power from within a unit solid angle from a unit emitting area and unit wavelength” scaled by the device’s surface area A [24]. In other words, Equation 2.16, calculates the flux density of the radiation emitted by the device and multiplies it by its surface area A .

$$P_{rad}(T_{dev}) = A \int_0^\infty I_{bb}(T_{dev}, \lambda) \epsilon_{dev}(\theta, \lambda) d\lambda \int \cos(\theta) d\Omega \quad (2.16)$$

In the above equation, the device’s blackbody radiation I_{bb} , which is calculated at the device temperature, is scaled by the emissivity of the device $\epsilon_{dev}(\theta, \lambda)$. This value is both wavelength λ dependent and incident angle θ dependent.

This product is then integrated over all angles in the hemisphere using $d\Omega$. Equation 2.17 calculates the solid angle; note that the solid angle $d\Omega$ in 2.17 allows $P_{rad}(T_{dev})$ to integrate over the intensity of radiation emitted over the hemisphere in all directions.

$$d\Omega = \sin(\theta) d\theta d\phi \quad (2.17)$$

The $\cos(\theta)$ term restricts all radiation to the vertical direction. The following simplifications are made from Equation 2.17.

$$\begin{aligned} d\Omega &= \sin(\theta) d\theta d\phi \\ \int d\Omega &= \int_0^{2\pi} \int_0^{\pi/2} \sin(\theta) d\theta d\phi \\ &= 2\pi \int_0^{\pi/2} \sin(\theta) d\theta \end{aligned} \quad (2.18)$$

Therefore Equation 2.16 can simplify to the following:

$$P_{rad}(T_{dev}) = 2\pi A \int_0^{\pi/2} \left[\int_0^\infty I_{bb}(T_{dev}, \lambda) \epsilon_{dev}(\theta, \lambda) d\lambda \right] \sin(\theta) \cos(\theta) d\theta \quad (2.19)$$

Ideally, the power radiated from the device is not absorbed by the atmosphere because the radiation is emitted over the atmospheric window.

2.7.2 Radiation power density absorbed from the sun

While $P_{rad}(T_{dev})$ works to lower the temperature of the surface by emitting radiation, solar radiation works to raise device temperature. $P_{sun}(\theta_{sun})$ represents the amount of solar radiation absorbed by the device. θ_{sun} is the angle with which the solar radiation hits the earth’s surface; it is taken to be constant and directly overhead the device, $\theta_{sun} = 0$

$$P_{sun}(\theta_{sun}) = A \int_0^\infty I_{AM1.5}(\lambda) \alpha_{dev}(\theta_{sun}, \lambda) d\lambda \quad (2.20)$$

$I_{AM1.5}$ is the solar intensity spectrum, which calculates the total solar intensity at earth's surface at each wavelength. Hence, the solar radiative power absorbed by the device is calculated by scaling the $I_{AM1.5}$ spectrum by the amount of radiation that is absorbed at each wavelength. Due to Kirchhoff's Law, Equation 2.6, which states that emissivity is equal to absorption, the emission term in the Equation 2.16 is replaced with an absorption term. The data used in calculating this equation remains the same.

2.7.3 Radiation power density absorbed from the atmosphere

The device also absorbs radiation that is re-emitted from the atmosphere towards the earth's surface.

$$\begin{aligned} P_{atm}(T_{amb}) &= A \int \left[\int_0^\infty I_{bb}(T_{amb}, \lambda) \epsilon_{atm}(\theta, \lambda) \alpha_{dev}(\theta, \lambda) d\lambda \right] \cos(\theta) d\Omega \\ P_{atm}(T_{amb}) &= 2\pi A \int_0^{\pi/2} \left[\int_0^\infty I_{bb}(T_{amb}, \lambda) \epsilon_{atm}(\theta, \lambda) \alpha_{dev}(\theta, \lambda) d\lambda \right] \sin(\theta) \cos(\theta) d\theta \end{aligned} \quad (2.21)$$

$I_{bb}(T_{amb}, \lambda)$ is the blackbody spectrum of atmosphere at the earth's surface. The $\epsilon_{atm}(\theta, \lambda)$ term represents the atmosphere's emissivity and $\alpha_{dev}(\theta, \lambda)$ is the device's emissivity. The product of $I_{bb}(T_{amb}, \lambda)$ and $\epsilon_{atm}(\theta, \lambda)$ yields the total output power emitted by the atmosphere. $\alpha_{dev}(\theta, \lambda)$ narrows value of the power to include only what is absorbed by the device. Similar to $P_{rad}(T_{dev})$, $d\Omega$ integrates this function over all hemispheric angles while $\cos(\theta)$ limits the output to the direction normal to the beam of light.

Note, that as the concentration of greenhouse gases in the atmosphere rises, their radiative forcing will cause $P_{atm}(T_{amb})$ to rise. Therefore, by emitting radiation over the atmospheric window, PDRC devices limit how much radiation they contribute to this term.

2.7.4 Radiation power density absorbed from conduction and convection

Equation 4.5 captures the parasitic heat gain due to the PDRC's contact with other surfaces and due to adjacent air flow.

$$P_{cond+conv}(T_{dev}, T_{amb}) = Ah_c(T_{amb} - T_{dev}) \quad (2.22)$$

h_c is the thermal coefficient and can be experimentally measured. Previous experiments have measured this value to be $10 \frac{W}{m^2*K}$ for a 4 in silicon wafer [27].

2.8 Summary of Passive Daytime Radiative Cooling

PDRC devices achieve sub-ambient cooling by maximizing $P_{rad}(T_{dev})$ and minimizing $P_{sun}(\theta_{sun})$, $P_{atm}(T_{amb})$, and $P_{cond+conv}(T_{dev}, T_{amb})$. In order to limit the transfer of radiation from $P_{sun}(\theta_{sun})$, PDRC devices must be highly reflective in the visible range, the wavelength region over which half of the sun's total power is radiated. PDRC devices should also emit radiation over the atmospheric window so that their radiation does not contribute to atmospheric heating or to the radiation that could be re-reflected by the atmosphere to the earth's surface (accounted for in the $P_{atm}(T_{amb})$ term). Therefore, to achieve cooling, PDRC devices must emit enough blackbody radiation over the atmospheric window to overpower the radiative transfers from $P_{sun}(\theta_{sun})$, $P_{atm}(T_{amb})$ and $P_{cond+conv}(T_{dev}, T_{amb})$. The fabrication process for these devices is described in the following section.

Chapter 3

Experimental Methods

This chapter details the experimental device fabrication, rooftop testing design, and spectra measuring procedure undertaken for this project in the Hudgings Lab. Additional details about procedures can be found in the appendix.

3.1 Device Structures

Passive daytime radiative cooling devices must be highly reflective at visible wavelengths and highly emissive at infrared long wavelengths, specifically between $8\mu\text{m}$ and $13\mu\text{m}$ in order to achieve sub-ambient cooling. This project uses silver (Ag), which has an average of 98% reflectivity in the visible range, and Polydimethylsiloxane (PDMS), which has on average 94% emissivity in the IR. Our device structure is adapted from Kou et al. and Zhou et al., which both used layered substrates consisting of PDMS [27] [49]. Kou et al. used a fused silica base substrate top-coated by a layer of PDMS and bottom-coated with a layer of silver [27]. Zhou et al. used an aluminum substrate covered in a silver and a PDMS layer [49].

Figure 3.1 depicts these two devices, which were used in this experiment. Device a) consists of a Silicon (Si) wafer substrate, a layer of $120\mu\text{m}$ of thermally evaporated silver (Ag), followed by $500\mu\text{m}$ of PDMS. Device b) consists of a Fused Silica (FS) wafer substrate, with $500\mu\text{m}$ of Polydimethylsiloxane (PDMS) on the top side, and $120\mu\text{m}$ of thermally evaporated silver on the bottom. The Si wafer substrate is opaque, whereas the FS is transparent to the human eye. Constructing and experimenting with these two variations allows us to examine device characterization and performance across the different wafer substrates.

3.2 Device Fabrication

Device fabrication involves three main steps. (1) First, the base material, either FS or Si, is cleaned in the plasma cleaner, (2) then $120\mu\text{m}$ of Ag is deposited with a thermal evaporator, and (3) finally $500\mu\text{m}$ of Polydimethylsiloxane (PDMS) is blade coated onto the

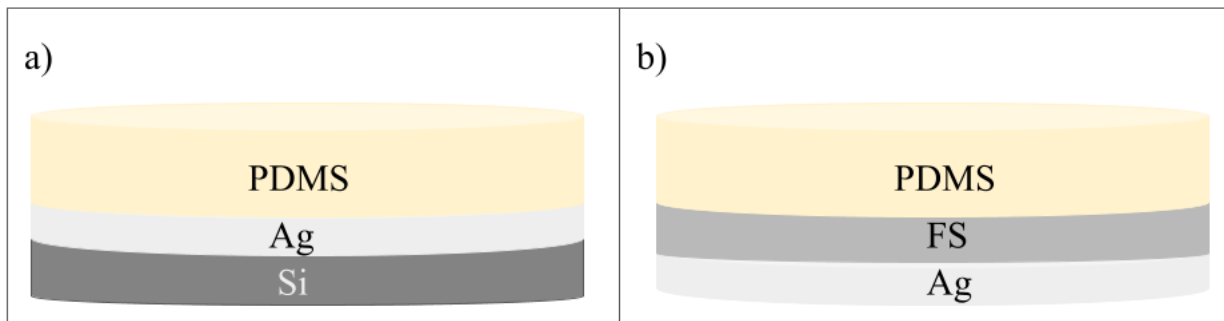


Figure 3.1: Figure a) shows the cross-section of the Silicon (Si) based devices and figure b) shows the cross-section of the Fused Silica (FS) based devices

device. We fabricate these devices in the Chem Prep Lab located in Estella Basement on Pomona College's campus.

Wafer Cleaning

Both the Si and FS wafer substrates are 100cm in diameter and 500 μm thick. They are stored in dust-free containers prior to any thin-film depositions. Each wafer is plasma cleaned in the Harrick Plasma PDC001-HP plasma cleaner for three minutes prior to thin film deposition in order to eliminate any organic contaminants on the wafer surface. Each wafer is cleaned one at a time due to size constraints of the plasma cleaner. Specific instructions for the plasma cleaner can be found in the Chem Prep Lab in a binder next to the plasma cleaner.

Thermal Evaporation

Once organic material has been removed from the base wafers, an Angstrom Engineering NexDep System thermal evaporator is used to thermally evaporate 120 μm of silver (Ag) under vacuum pressure onto the wafers. This thin layer of Ag serves as the highly reflective and thermally conductive layer on the device.

To perform the thermal evaporation, wafers are mounted onto a base plate, which holds them securely in the thermal evaporator. Wafers are mounted onto a base plate using four triangle screws; the edges of the screws fasten the wafer to the plate. In order to keep track of the side of the wafer with silver, turn all screws counterclockwise. This ensures that when the Ag is deposited, there are four asymmetric small triangle shaped edges on the Ag side of the wafer (where Ag is not deposited). This surface area on which the Ag is not deposited is a small percentage of the wafer's total surface area and is therefore assumed to have a negligible impact on device performance. Thermal evaporation occurs one wafer at a time due to the size constraints of the base plate and thermal evaporator. Specific instructions for how to operate the thermal evaporator are located in a binder next to the device in the

Chem Prep Lab.

PDMS curing

Polydimethylsiloxane (PDMS), a non-toxic and relatively inexpensive silicone organic polymer, acts as the emissive layer on the devices. We use the Sylgard 184 kit to make PDMS, which includes two substances: the elastomer base and curing agent. In order to make PDMS, the elastomer base is mixed with the curing agent at a 10:1 base-to-curing agent ratio. PDMS cures at room temperature and therefore cannot be left overnight. Still, once the base and curing agent are sufficiently mixed using a stirring rod, the PDMS must sit in the fume hood for a minimum of three hours to allow any air bubbles trapped in the fluid to dissipate prior to blade coating. PDMS preparation can take place prior to plasma cleaning if time allows.

Blade Coating

PDMS is blade coated onto the wafers using a Teflon spatula and a cardboard template measured and laser cut to be 500 μm thick and 98mm in diameter.¹

To ensure that the template is reusable, a thin piece of wax paper, cut to the same diameter, is placed over the template during the blade coating process. Once the template and wax paper are in place, PDMS is poured from the boat onto the top half of the wafer. In order to ensure that the entire wafer will become blade coated with PDMS, a thin amount of the PDMS is also poured on the outer edge of the wafer. Next, in one movement, the spatula is pulled across the wafer starting from the top of the wafer down at a constant speed. A uniform layer of PDMS is best accomplished with one swipe of the spatula. If the wafer is not uniformly covered, a pipette is used to fill in the gaps. Pulling the spatula across the wafer again smudges the PDMS that is already in place on the wafer.

Once blade coated, place the wafer on a hot plate at 100°C for 45 minutes in order to let the PDMS solidify. Heating up the wafer expedites the curing process. Alternatively, allowing the PDMS to set at room temperature risks altering the thickness of the layer because the liquid PDMS has the potential to drip off the wafer as it cures over the longer time period.

3.3 Outdoor Rooftop Testing

Device temperatures are tracked in both day and nighttime settings on the top of Dialynas roof on Pomona College's campus in Claremont, CA. Each complete PDRC device is measured against two controls, a blank wafer, and a wafer coated with Ag. The ambient temperature is also tracked. Daytime testing takes place during peak sunlight hours between

¹The template is 98cm in diameter to ensure that PDMS does not spill over the side of the 100mm wafer substrate.

10am and 3pm. Nighttime testing occurs after sunset and helps differentiate between the impact of the reflective layers and cooling that results from the emissive layers.

Test Stands

Device stands, designed by Paul McKinley '22, are 3D printed from translucent polylactic acid filament with polystyrene thermal insulation beds in order to limit parasitic heating via conduction from the surrounding environment. The wafer sits on top of the insulating bed. Each thermocouple is wired up through the polystyrene insulation so that they make direct contact with the back of the wafer. Thermal paste is applied to the top of the thermocouple to ensure that the wafer has good contact to the thermocouple.

Temperature Probes and Data Logger

Initial rooftop testing, designed by Paul Mckinley'22, used TMP36 analog temperature sensors, an Arduino microcontroller, and data logger shield attachment. TMP36 temperature sensors measure the voltage drop across a diode, which is directly proportional to the change in temperature. These probes, which are connected via soldered wires to the breadboard, make direct contact with the back of the wafer and sit atop the polystyrene insulation in the wafer stand. However, these temperature sensors collected data in 0.5°C steps. Therefore, this new testing setup can measure more sensitive changes in temperature.

To address this concern, we modified the setup such that device temperature is tracked and logged using T-type thermocouples and a 4 Channel Reed Series Data Logger R2450SD. T-type thermocouples use the difference in voltage generated at the contact point between two wires of Copper and Constantan to measure temperature using a well established conversion factor. These thermocouples have a temperature range of -100°C to 400.0°C and measure temperature with a 0.1°C resolution. Each thermocouple has a flat soldered edge so that it makes direct contact with the back of the wafer.

Table 3.1: Accuracy ranges for T-Type Thermocouples by temperature [1]

Temperature	Accuracy $\Delta V(mV)$
-148.0 to -58.1°F	$\pm 0.4\% + 1.8^{\circ}\text{F}$
-58.0 to 752.0°F	$\pm 0.4\% + 1^{\circ}\text{F}$
-100.0 to -50.1°C	$\pm 0.4\% + 1^{\circ}\text{C}$
-50.0 to 400.0°C	$\pm 0.4\% + 0.5^{\circ}\text{C}$

The data logger can track up to four temperatures at once from four separate thermocouples. While the data logger has a stand alone battery, the current testing location does take advantage of an external power outlet. During data collection, the data logger stores the temperature readings to an SD card on a csv file.

Data Logger Procedure

Stands, thermocouples, and data logger are placed in direct sunlight (for daytime testing) on the top of Dialynas roof. Once wafers and the ambient probe are secure on the stands, the four thermocouples are connected to the inputs located on the top of the data logger labeled T1 to T4. Four temperatures will be displayed on the data logger if all thermocouples are appropriately connected to the data logger and wafers. The full PDRC wafer and controls are rotated among the four different thermocouples after each experimental run to ensure that any temperature readings are not an inherent product of the thermocouples. Therefore, prior to each experiment, a record is made of which wafer corresponds to which input. The "Set Time" button is used to set the sampling rate to 30 seconds. Once the SD card is inserted, the LOG button is held for 2 seconds to begin recording data. The logger button will begin flashing when data is actively being logged. See data logger manual linked in the appendix for further instructions on how to record and log data. To end the data logging session, press and hold log button. All data is stored to an SD card in a single excel file.

Temperature Probe Calibrations

Figure 3.2 shows the results of the temperature calibration experiment to used confirm that the probes read accurate temperatures and are consistent with each other. We placed the probes in a beaker of ice water and placed the beaker on a hot plate. Then, we turned the hot plate on until the water boiled. Note the initial divergence in temperatures is due to time it takes for the heat to become uniformly distributed within the beaker.

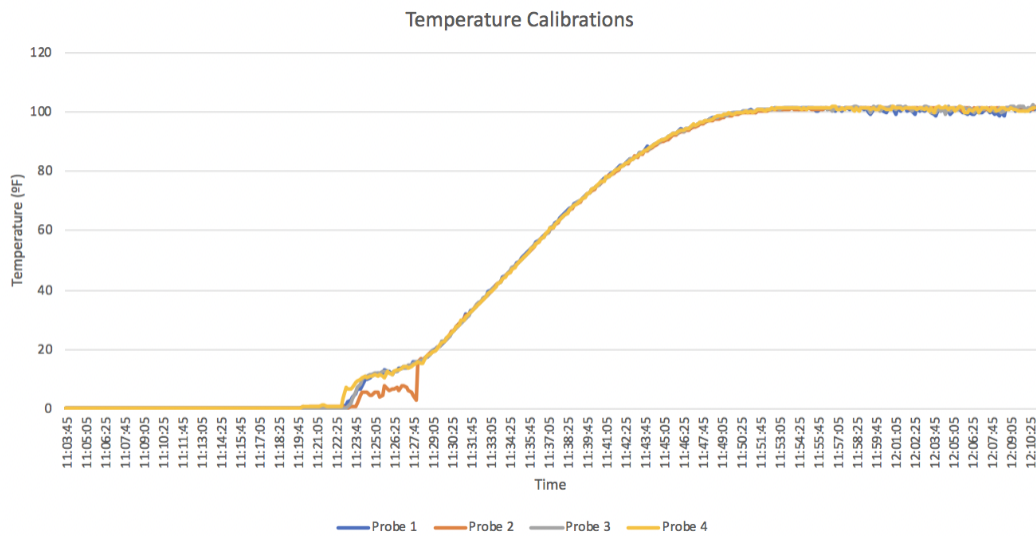


Figure 3.2: Graph of temperature probe calibrations.

3.4 Outdoor Set Up Robustness Testing

This section details testing and additional adjustments made to the initial fabrication and outdoor testing setup designed by Paul McKinley.

3.4.1 Device Fabrication

Layering Test

The structure of the silicon PDRC device differs slightly from the structure of the fused silica PDRC device. The silicon-based device has the PDMS deposited on top of the silver evaporated layer. In contrast, in the fused silica device, the PDMS is deposited directly on top of the fused silica wafer and the silver is evaporated onto the bottom of the wafer. The initial reasoning for this was based on the idea that fused silica has some emissive properties and depositing silver on top of the surface would interfere with the fused silica's characteristics.

To confirm this, we performed a rooftop experiment that compared the cooling capacity of two fused silica devices. The first device (device a) is our initial structure; a fused silica base with a PDMS topcoat and an evaporated silver bottom layer. The second device switches the order of the fused silica and silver layers.

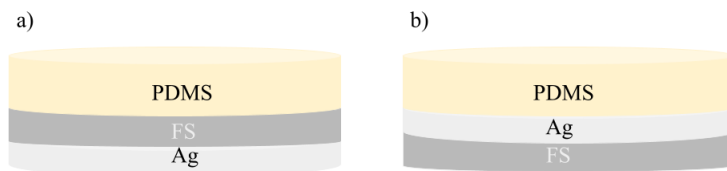


Figure 3.3: Shows cross section of tested devices

The results of a daytime rooftop experiment are shown in Figure 3.4. We find that the initial design, device a, achieves a slightly better level of cooling than device b. Therefore, the initial structure of the fused silica device is superior. Note we cannot compare device performance to ambient temperature due to the fluctuation in its temperature. Additional discussion on measuring ambient temperature can be found later in the chapter.

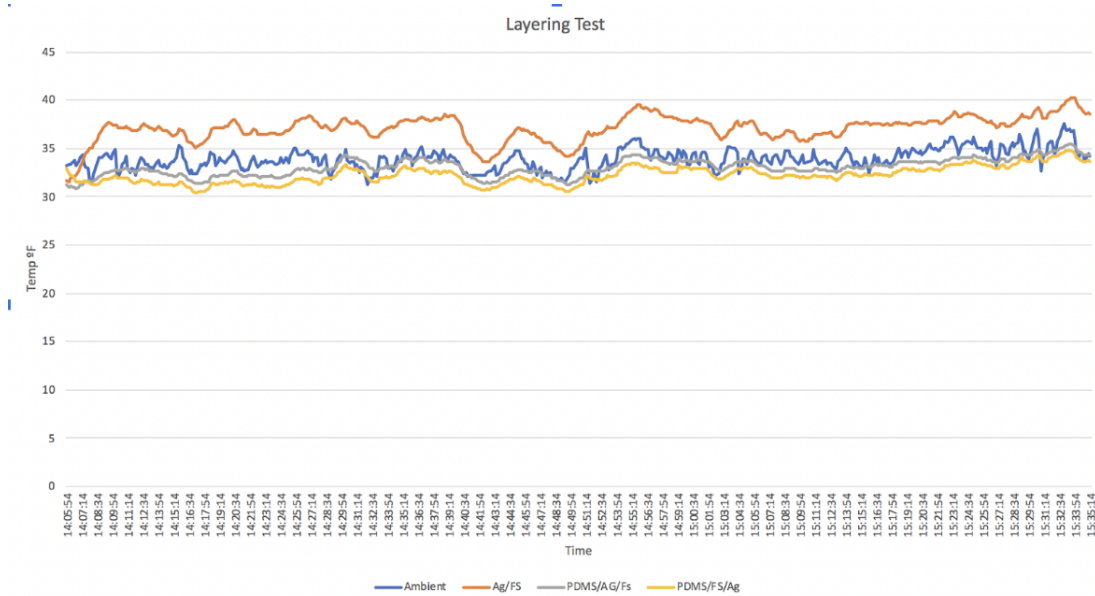


Figure 3.4: Graph of rooftop experiment testing the structure of the fused silica device.

PDMS Thickness

We also conducted a test to confirm the proper thickness for PDMS. We tested three different thicknesses 200 μm , 500 μm , and 950 μm with our rooftop setup; this data is shown in Figure 3.5.

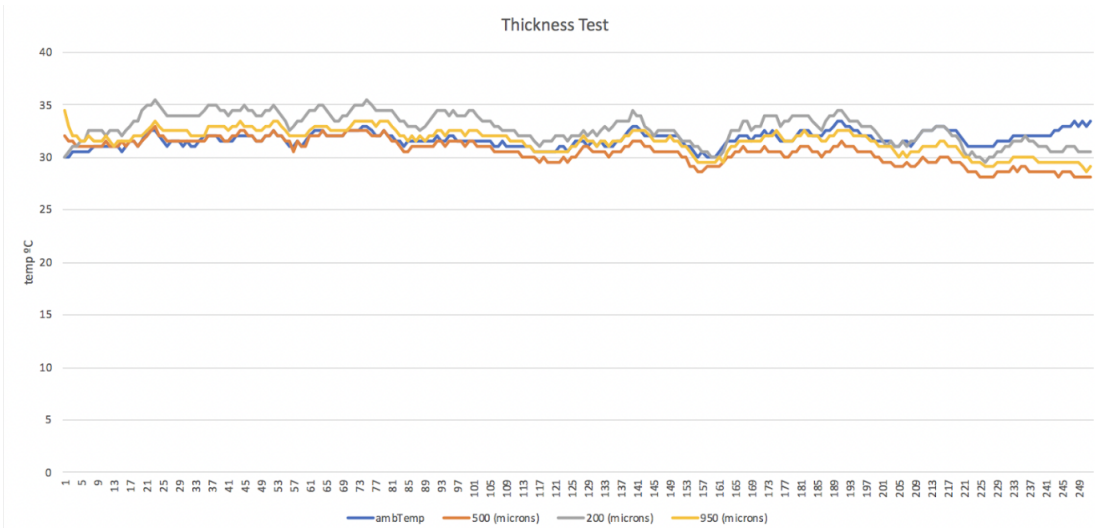


Figure 3.5: Graph of rooftop experiment testing varying PDMS thicknesses.

The 500 μm thickness performed better than 200 μm and 950 μm confirming the original structure. This outdoor testing setup was conducted with the Arduino micro-controller and

TP36 temperature probes. Note the step-like structure to the graph. This is a result of Arduino only recording the temperature in discrete 0.5°C steps.

3.4.2 Measuring Ambient Temperature

In Figures 3.4 and 3.5, the ambient temperature reading is fluctuating too significantly to properly quantify the reading. This fluctuation led us to an in-depth examination of how to measure ambient temperature.

Measuring ambient temperature is surprisingly challenging. A thermocouple can absorb solar or thermal radiation and give a false reading, so the probe must be sheltered from the sun and the hot rooftop. However, a simple enclosure will trap hot air and heat up in the sun. Therefore, there are specific criteria that must be met in order to accurately measure ambient temperature set forth by the National Institute of Standards and Technology [8].

1. The temperature probe must be in a shaded enclosure with slatted side to allow air flow and to protect it from the elements.
2. The enclosure must be between 1.2 and 2 meters from the ground over dirt or short grass.
3. The enclosure must be away from trees, buildings, and pavement.

Currently, we are constructing this enclosure, modeled after the Stevenson Screen invented by Thomas Stevenson in the 19th century, to enclose the ambient probe [8]. Tag Curwen has been spearheading this construction with the help of Hardy Richardson. A reference Stevenson Screen structure is pictured below. Future outdoor testing will use this enclosure to measure ambient temperature as well as the new thermocouples.



Figure 3.6: Reference picture of a Stevenson Screen [39].

3.5 Spectral Measurements

This section details the procedure for how to measure the two main inputs for the python model: the device's emissivity and the device's specific heat capacity. The section also includes the measured and calculated spectral data and specific heat capacity values for each device.

3.5.1 Procedure

In order to use the power balance equations, reflectivity, transmissivity, and emissivity spectral data is required for each PDRC device and various controls. Once reflectivity and transmissivity spectra are acquired within the desired wavelengths, .34 μm to 25 μm , Equation 2.2 and Equation 2.6 are used to calculate the desired emissivity spectrum. The spectral data is then inputted through a python model, which calculates the power balance equations described in the Theory section to find the device's total change in temperature.

There are three pieces of equipment involved in measuring the spectral properties of these devices. The Cary 300 Bio UV-Visible Spectrophotometer located in the Pomona College Chemistry Department and the OceanOptics USB2000+ spectrometer located in the Pomona College Physics Department are used to measured transmissivity data between 340nm and 900nm and reflectivity data between 340nm to 1029nm respectively. A Nicolet is50 Fourier-transform infrared (FTIR) spectrometer located in the Chemistry Department is used to measure transmissivity and reflectivity data in the IR, between wavelengths 2.5 μm to 25 μm .

Measuring Reflectivity Data in the Visible

Reflectivity data in the visible range is captured using the OceanOptics USB2000+ spectrometer. This experimental set up is in Estella basement in Professor Hudgings' lab. The following procedure details the step for measure the reflectivity of an individual wafer. Ocean Optics has an option for measuring reflectivity; however, this feature requires a certain reference sample that was not accessible at the time this thesis was written.

Once the computer is turned on, open OceanView 1.6.7 Software and select "quick view." An intensity spectrum should be displayed. The following four measurements are imported to an excel sheet.

1. B_1 Background measurement with a mirror while the source light is off.
2. I_1 Spectrum measurement with mirror while the source light is on.
3. B_2 Background measurement with the sample with the source light off.
4. I_2 Spectrum with the sample with the light source on.

Once this data is imported into an excel sheet, the following equation is used to calculate the reflectivity of the sample with the known reflectivity of the mirror $R_{mirror} = .98$.

$$\begin{aligned} I_{light} &= \frac{I_1 - B_1}{R_{mirror}} \\ R_{sample} &= \frac{I_2 - B_2}{I_{light}} \end{aligned} \quad (3.1)$$

Note that for samples coated with Ag, but not PDMS, the surface reflectivity in the visible was assumed to be 98% over the visible range. This is due to the fact that Ag coated surfaces are more reflective than the mirror. This assumption is consistent with data from the literature [38].

Measuring Transmissivity Data in the Visible

Transmissivity data over visible wavelengths is measured using the Cary 300 Bio UV-Visible Spectrophotometer located in the Pomona College Chemistry Department. This UV-Vis Spectrophotometer can acquire measurements from 190nm - 900nm. However, given the OceanOptics spectrometer is limited to 340nm, data acquisition can begin at 340nm for the transmissivity data. Each transmissivity measurement must be taken individually. Specific instructions for how to set acquisition parameters are located next to the equipment.

Transmissivity measurements require an initial background spectrum. Close the hood and click the "zero" button to take the background spectrum. This background does not need to be repeated for each individual sample. For our measurements, the background sample is air. Once the background is taken, insert the 3D test sample into printed stand pictured below and begin taking sample measurements. Specific instructions for how to save the files are located in the instruction manual next to the machine.

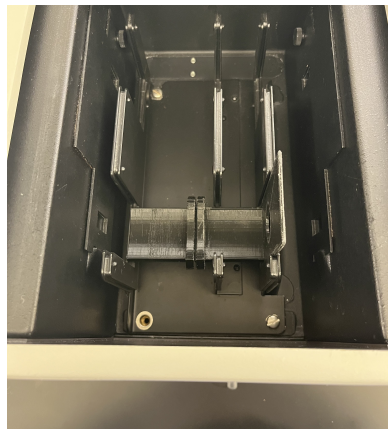


Figure 3.7: Picture of the Uv-Vis testing apparatus and 3D printed wafer stand.

Measuring Reflectivity Data in the IR

Reflectivity data in the infrared range, from $2.5\mu\text{m}$ to $25\mu\text{m}$, is captured with the Nicolet iS50 Fourier-transform infrared (FTIR) spectrometer using the 10-degree specular reflection accessory (10Spec) located in the Chemistry Department. This accessory measures reflectivity at a near normal angle. A detailed instruction manual is in the appendix. The 10Spec accessory is not left in the FTIR machine. Specific instructions for how to insert the 10Spec accessory can also be found in the appendix.

Once the accessory is in place, start the “OMNIC” software from the desktop. Place the mask in the groove of the 10Spec. Similar to the visible measurements, reflectivity measurements require a background to be taken. Background measurements are taken with a gold plate. Ensure the gold is facing gold-side down on the mask. Hit ”col bkg” to collect a background measurement of the gold plate. Select ”add to window.” Replace gold plate with sample and select ”col smp” to take your measurement. Once again select ”add to window” and repeat until all samples are collected.

Note the FTIR machine measures in wavenumber cm^{-1} . All data is converted into wavelength using excel.

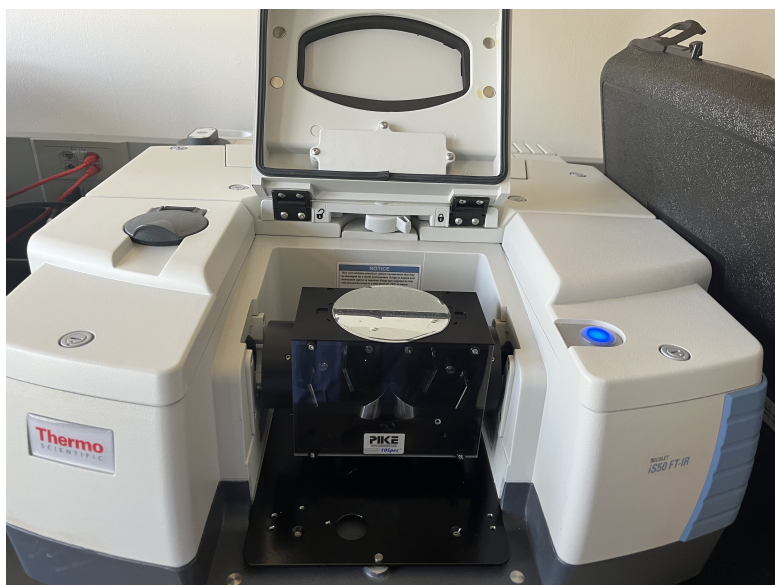


Figure 3.8: Picture of the FTIR reflectivity testing setup with 10Spec.

Measuring Tranmissivity Data in the IR

Tranmissivity data is also captured using Nicolet is50 Fourier-transform infrared (FTIR) spectrometer. However, there is no accessory involved. Following the instructions to switch out the modules located in the appendix, tranmissivity measurements are captured following the same procedure as above. The 3D printed stand used in the Cary 300 Bio UV-Visible Spectrophotometer is also used for tranmissivity measurements with this equipment. Air is used as the background.

3.5.2 Spectral Data

As noted above, we measure reflectivity $\rho(\lambda)$ and transmittivity $\tau(\lambda)$ of the two PDRC devices and the four controls. Note there is a gap in the measured spectral data between 1200nm and 2500nm due to the measuring ranges of our instruments. The data is interpolated between these ranges. To calculate absorptivity, we rearrange the conservation law in equation 2.2 to obtain:

$$\alpha(\lambda) = 1 - \rho(\lambda) - \tau(\lambda) \quad (3.2)$$

By Kirchhoff's law, Equation 2.6, at thermal equilibrium absorptivity and emissivity are equal. Hence from the calculated absorptivity, we calculate emissivity.

Silicon Based Devices

The silicon substrate used in this experiment is an opaque wafer that looks nearly black. As expected, the reflectivity of the wafer ranges from 20% to 55% over the measured spectrum, while transmissivity is 0% to significant figures. Reference data was used for the reflectance spectrum for the bare silicon wafer in the visible range from 340nm to 1200nm.² Tranmissivity data and reflectivity data in the IR for the bare silicon wafer were captured using the methods laid out in chapter 3.

From these two spectra we calculate the following absorptivity and emissivity spectrum. The average emissivity of bare silicon is found to range from 45-80%. Once silver is deposited on the wafers, the reflectivity dramatically increases, decreasing the absorptivity and emissivity values. Average reflectivity is 99%. Tranmissivity remains at zero. Average absorptivity and emissivity is 1%.

Blade coating 500 μm of PDMS onto the silver-coated Si wafer causes the emissivity of the device to rise again. While it would be natural to conclude that silver reduces overall performance of the PDRC device, it is important to remember that there are two main characteristics of a passive daytime radiative cooler. (1) It must be highly reflective in the visible and (2) highly emissive in the atmospheric window 8 μm to 13 μm (8000 - 13000nm).

²Visible reflection data for Blank Si is extracted from the following reference:<https://www.researchgate.net/figure/Reflection-of-the-prepared-GNP-deposited-Si-GNP-Si-and-a-blank-Si-waferfig5327297172>

Figures 3.13 and 3.14 show that the silicon PDRC device fits these criteria. The device's reflectivity is high in the visible wavelengths, averaging 97% between 340nm and 900nm. The emissivity is high in the IR, averaging 85% between 2500nm to 25,000nm.

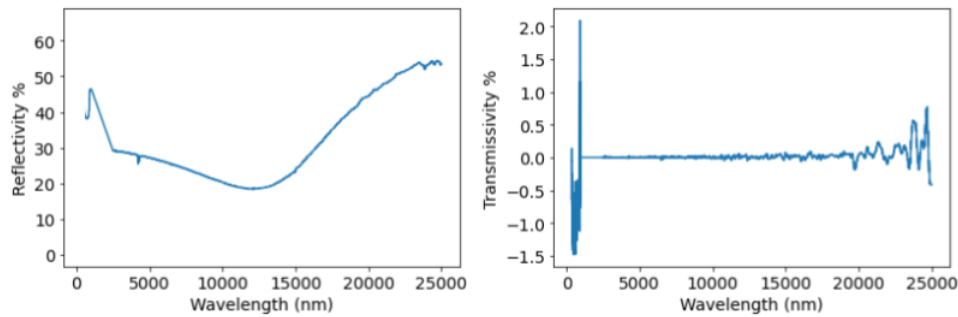


Figure 3.9: Reflectivity and measured transmissivity spectra of bare Si wafer.

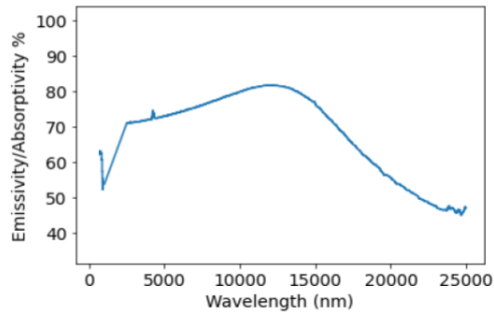


Figure 3.10: Absorptivity and emissivity spectra of bare Si wafer.

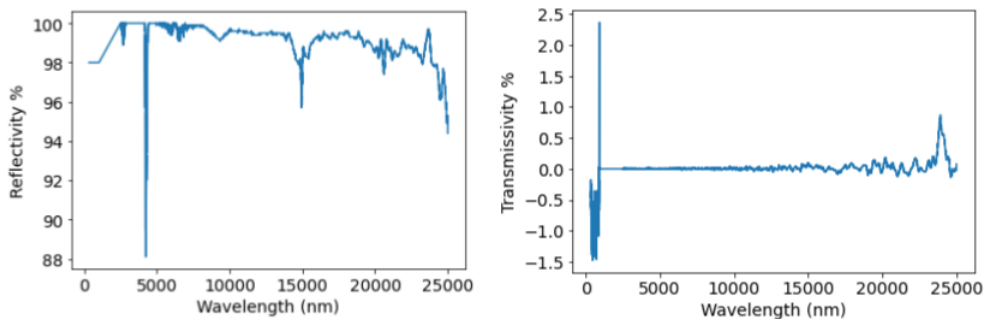


Figure 3.11: Measured reflectivity and transmissivity spectra of silver-coated silicon.

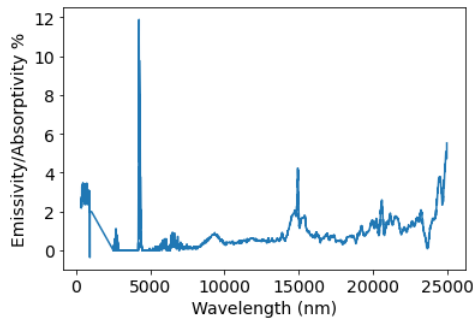


Figure 3.12: Absorptivity and emissivity spectrum of silver-coated silicon.

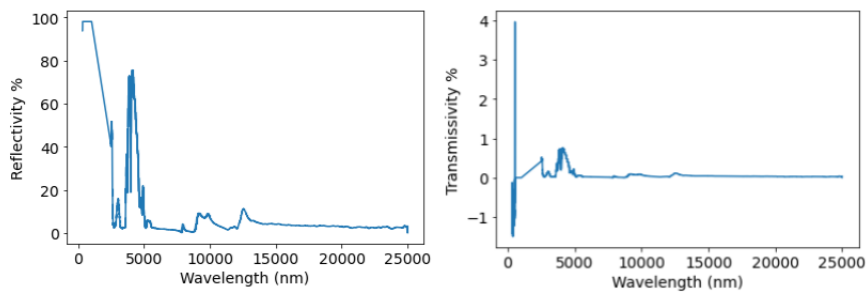


Figure 3.13: Measured reflectivity and transmissivity spectra of PDRC Si device.

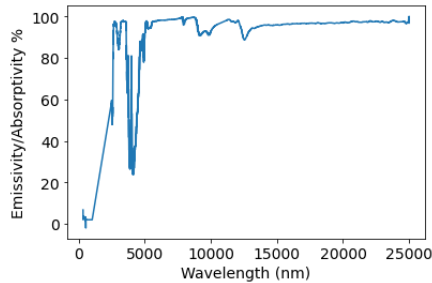


Figure 3.14: Absorptivity and emissivity spectrum of PDRC Si device.

Fused Silica Based Devices

Bare fused silica, unlike silicon, is transparent to the human eye. Thus, transmissivity is high (94%) in the visible wavelengths, yet dramatically drops off in the IR. Additionally, bare fused silica has a sharper reflectivity peak than silicon. However, average reflectivity is lower, 10%. For the bare wafer, the absorptivity and emissivity are low (0%) in the visible but increases to 77% in the atmospheric window.

Once we deposit 120 μ m of silver on the fused silica, reflectivity rises to 98% and transmissivity falls to zero. As a result, emissivity and absorptivity similarly fall to an average value of 1%. Depositing PDMS onto the silver coated fused silica wafer dramatically increases the

emissivity of the device. Reflectivity remains at the 98% level in the visible (between 340nm to 900nm) but falls to 6% in the atmospheric window. Emissivity remains low at 2% in the visible, then increases to 94% in the atmospheric window (8000nm to 13000nm).

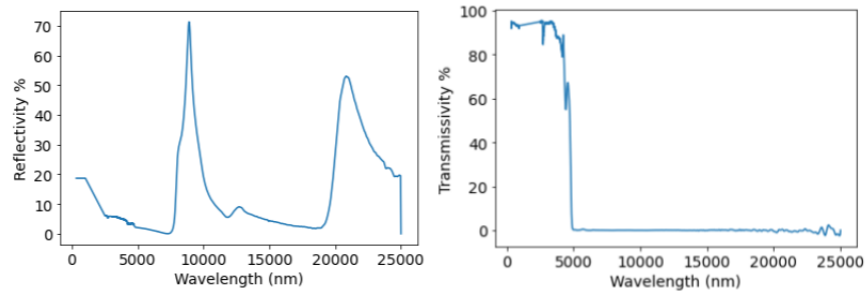


Figure 3.15: Measured reflectivity and transmissivity spectra of bare fused silica wafer substrate.

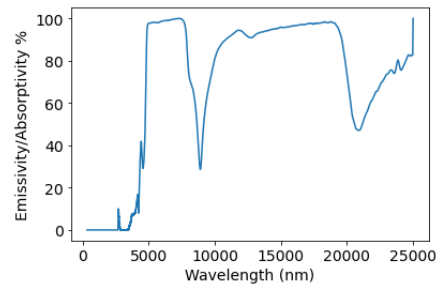


Figure 3.16: Absorptivity and emissivity spectrum of bare fused silica wafer substrate.

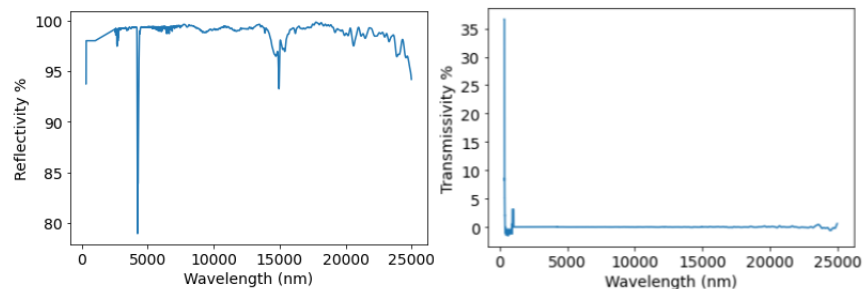


Figure 3.17: Measured reflectivity and transmissivity spectra of fused silica wafer with Ag.

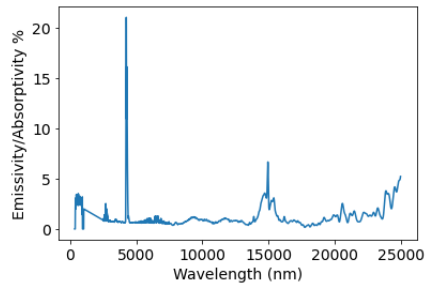


Figure 3.18: Absorptivity and emissivity spectra of fused silica wafer with Ag.

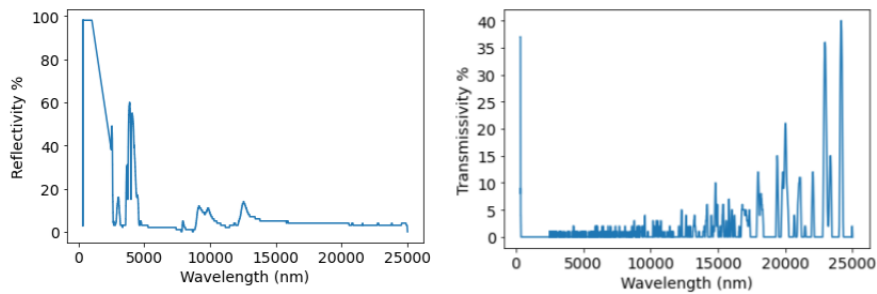


Figure 3.19: Reflectivity and transmissivity spectra of fused silica PDRC device.

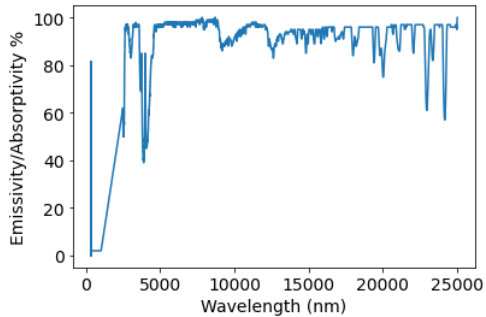


Figure 3.20: Absorptivity and emissivity spectra of fused silica PDRC device.

3.5.3 Summary

This section details procedure for collecting spectral data as well as the measured spectra for the silicon, fused silica devices, and various controls. The devices' spectral characteristics allow us to explain how devices lower their temperature below ambient. When the device is highly reflective in the visible range, it limits the amount of absorbed solar radiation, minimizing the amount of heat absorbed in the visible wavelengths. When the device is highly emissive, particularly in the atmospheric window, it is more efficient at dissipating its thermal energy to the atmosphere and into space. We see high reflectivity values in the visible and high emissivity values in the IR for both the silicon and fused silica PDRC devices.

Therefore, these devices fit the desired characteristics for a passive daytime radiative coolers and we should expect to see sub-ambient cooling.

3.6 Specific Heat Capacity Measurements

The power balance equation models the PDRC devices' output power in watts. Yet, to fully understand the cooling capacity of the devices, this rate of energy transfer must be converted to a change in temperature of the device. The following equation, 3.3, is used to calculate the rate at which each device changes its temperature using an experimentally measured heat capacity. q is thermal energy measured in joules, m is mass in kg, c is the specific heat capacity in $J/(kg*K)$, and ΔT is the change in temperature in K.

$$q = m * c * \Delta T \quad (3.3)$$

The specific heat capacity c is experimentally measured by sandwiching a Peltier cooler between an aluminum block and our test device. As the Peltier cooler moves thermal energy from the Al block to the test device (or vice versa), the temperature of both the block device is measured over time.

The thermal energy removed from the Al block is equal to the thermal energy gained by the test device. Therefore, we can make the following relation from equation 3.3.

$$\begin{aligned} m_{Al} * c_{Al} * \Delta T_{Al} &= m_{wafer} * c_{wafer} * \Delta T_{wafer} \\ c_{wafer} &= \frac{m_{Al} * c_{Al} * \Delta T_{Al}}{m_{wafer} * \Delta T_{wafer}} \end{aligned} \quad (3.4)$$

The following quantities are known: the mass of the Al block $m_{Al} = (0.372\text{kg})$, the mass of each device m_{wafer} measured with a balance, the specific heat capacity of the Al block $c_{Al} = (875\text{J/kg * K})$, and experimentally measured temperature changes for the Al block ΔT_{Al} and wafer ΔT_{wafer} .

To calculate specific heat capacity of each wafer, we need to experimentally measure how the wafer changes its temperature relative to the Al block with a known specific heat capacity. The procedure for experimentally setting up this experiment and measuring the relative temperature changes is detailed below. This procedure uses the experimental setup for the "Heat Engines and the Peltier Device" lab for Physics 42 [28].

1. Disconnect everything from the output terminals of the power supply. Turn the current down until CC lights up.
2. Connect a single banana cable to the positive and negative terminals of the power supply. Increase the current to 2.0A.
3. Pull the banana cable out and adjust voltage to 1.5V.
4. Turn off the power supply.

5. Disconnect the Al blocks from each other and set the Al block without the thermoelectric cooler off to the side.
6. Lay the remaining Al block with the thermoelectric cooler cooling facing upwards, ensuring that the measurement probe is secure in the block, and place the sample on top.
7. Place the measurement probe on the top side of the wafer and cover the waver with Styrofoam as shown in figure 3.21.
8. Connect the new "Peltier device" to the power supply via the red and black cables.
9. Using a LabQuest Mini, connect it to a lab computer and open Logger Pro. Go to the "Experiment" tab, "Data Collection." Set duration to 25 minutes and sampling rate to 30 samples/min. Check the "Continuous Data Collection" box.
10. Ensure that the temperatures are steady.
11. Click "start collection" while the power supply is off. Ensure that the temperatures are steady and then turn on the power supply.
12. Let the experiment run for 25 minutes. Using a slow heat transfer rate help to ensure that the temperature equilibrates across all layers of the device.
13. Run the experiment for each wafer and save as a .csv.
14. Import all data into excel and calculate the specific heat of each wafer using equation 3.4.

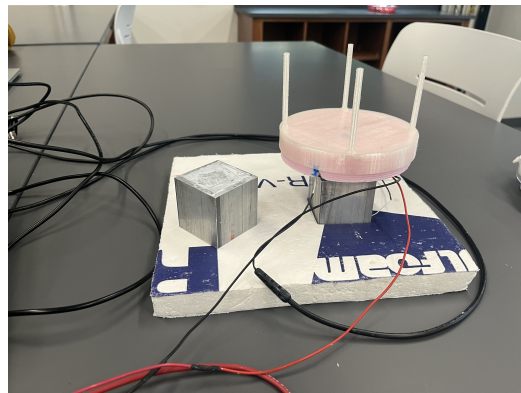


Figure 3.21: Picture of the Al block, Peltier Cooler, device, and Styrofoam setup.

3.6.1 Heat Capacity Results

The following table shows the results of the experiment laid out above. The last column shows the calculated heat capacity of each device using Equation 3.4. In this equation, m is mass, c is specific heat capacity, and ΔT is the recorded change in temperature of the Al block or the test device. The specific heat capacity of Al is 875 J/kg*K [28].

Equation 3.4 shows how we use the known specific heat of an aluminum block to calculate the unknown specific heat of our devices. Note that the change in temperature of the aluminum block is re-measured for each wafer.

Heat Capacity Experiment			
Wafer	Mass (kg)	ΔT (K)	Heat Capacity (J/Kg*K)
Si PDRC Al Block	.015 .327	9.12 -0.207	504 875
Si + Ag Al Block	.010 .327	-9.04 -.106	1590 875
Bare Si Al Block	.009 .327	-9.43 -0.363	1340 875
FS PDRC Al Block	.014 .327	9.12 -0.202	573 875
Fs + Ag Al Block	.009 .327	-11.2 -.171	814 875
Bare FS Al Block	.008 .327	-11.5 -.106	762 875

Table 3.2: Results from the heat capacity experiment detailed in the methods chapter.

The literature value for the specific heat capacity of silicon is 710 (J/kg*K) while fused silicon has been measured to have a specific heat capacity of 740 (J/kg*K) [21]. While the literature for fused silica is consistent with our measurement, our silicon heat capacity is larger. The silicon wafer has an electrically insulating thermal oxide layer SiO_2 , which would contribute to a higher value for specific heat capacity. Future work will investigate this discrepancy further.

3.6.2 Calculating change in device temperature

Using the experimentally measured specific heat c_{wafer} , we can use equation ?? again to calculate how the cooling power P_{cool} obtained from the power balance equations changes the temperature of the device T_{dev} :

$$\begin{aligned} P_{cool} &= m_{wafer} * c_{wafer} * \Delta T_{dev}/sec \\ \Delta T_{dev}/sec &= \frac{P_{cool}}{m_{wafer} * c_{wafer}} \end{aligned} \quad (3.5)$$

It is important to recognize that the power, P_{cool} , balance equations output a power measured in watts. Watts has Si units of Joules per second. Therefore, using equation 4.8, we find the device's change in temperature per second, not the overall change in temperature for the device. In order to properly model the device's behavior, we must account for this time factor by adjusting the device's temperature in the model over numerous iterations. Further discussion of the development of the model is described in the following section.

Chapter 4

Experimental Results

This results section focuses on the power balance model discussed in chapter 3. The power balance model accounts for the radiative transfers between the earth, atmosphere, and the sun that are responsible for heating and cooling the passive daytime radiative coolers. The main objective of this model is to determine how the passive daytime radiative coolers' temperature compares to ambient once the radiative transfers between the device and environment reach equilibrium. The main conclusions of this chapter discuss how the two PDRC devices perform relative to the tested control devices and to Paul McKinley's outdoor testing results. The chapter begins with a discussion of how to convert power from the power balance equations to a steady state temperature.

4.1 Development of Power Balance Model

Each device has a unique emissivity spectrum that allows it to convert thermal energy to radiation and dissipate its heat to the surrounding environment at a rate $P_{rad}(T_{dev})$.¹ Other sources from the sun P_{sun} , atmosphere $P_{atm}(T_{amb})$, and conduction and convection $P_{cond+conv}(T_{dev}, T_{amb})$ work to suppress the total cooling power of the device.² The power balance model calculates the cooling power P_{cool} of each device described in section 2.7 taking into account these various radiative power sources.

$$P_{cool} = P_{rad}(T_{dev}) - P_{atm}(T_{amb}) - P_{sun} - P_{cond+conv}(T_{dev}, T_{amb}) \quad (4.1)$$

The following sub-sections discuss the four radiative sources in the power balance model and how they impact device performance for the silicon PDRC device and bare silicon control.

¹ T_{dev} refers to the device temperature

² T_{amb} refers to the ambient temperature of the surrounding air

4.1.1 Power Radiated from the device: $P_{rad}(T_{dev})$

Each device emits blackbody radiation scaled by its unique emissivity spectrum. To confirm that our power balance model is properly calculating blackbody radiation, we compare our plot of spectral radiancy to the Eisberg and Resnick's plot below. Eisberg and Resnick's plot the spectral radiancy of a blackbody radiator at different temperatures [18].

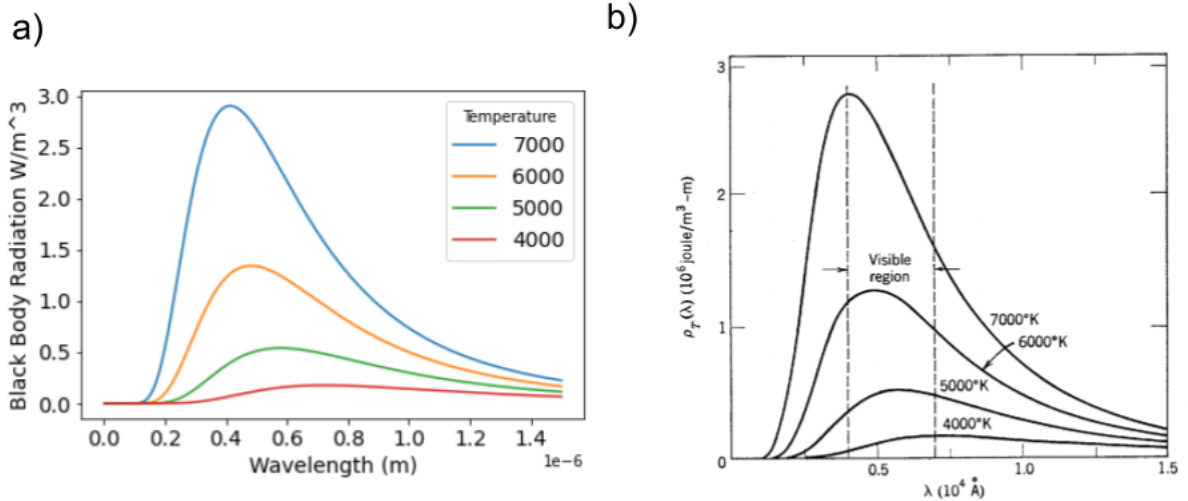


Figure 4.1: Blackbody Spectrum from power balance model relative to reference plot [18].

These two graphs are consistent along the y-axis. Note the Eisberg and Resnicks graph, figure b, is plotted in angstroms, while the power balance model is plotted against in m. Further note that the Eisberg and Resnicks is scaled by a factor of c and 4π steradians; our figure, figure a, accounts for this scaling factor.

Figure 4.1 is plotted for temperatures not seen in outdoor testing conditions. Therefore Figure 4.2 plots the blackbody spectrum $I_{bb}(\lambda, T_{dev})$ at temperatures close to ambient. Figure 4.2 shows that at cooler temperatures, blackbody radiation is significantly smaller, on the scale of 10^{-7} .

While these plots show radiance for a perfect blackbody, none of the tested devices are perfect blackbody radiators. Each device emits blackbody radiation that is scaled by their respective emissivity. Using the methods described in chapter 3, we measure spectral data for each device and input the calculated emissivity data $\epsilon_{dev}(\theta, \lambda)$ into equation 4.2 developed in chapter 2.

$$P_{rad}(T_{dev}) = 2\pi A \int_0^{\pi/2} \left[\int_0^{\infty} I_{bb}(T_{dev}, \lambda) \epsilon_{dev}(\theta, \lambda) d\lambda \right] \sin(\theta) \cos(\theta) d\theta \quad (4.2)$$

From this equation, we model how the $P_{rad}(T_{dev})$ changes for various device temperatures T_{dev} . Note A refers to the surface area of the device. The thermal radiation emitted by the

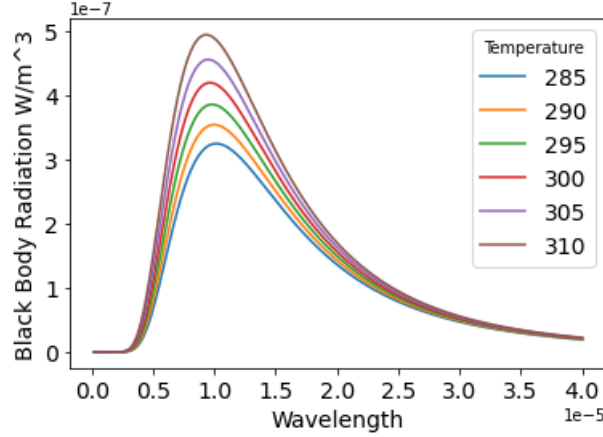


Figure 4.2: Black Body Spectrum at lower temperatures.

device scales with temperature. However, passive daytime radiative coolers ideally lower their temperature in presence of solar radiation over time. As the device temperature falls, so does its ability to radiate heat to the environment and continue cooling. Therefore, the devices are expected to eventually reach an equilibrium temperature.

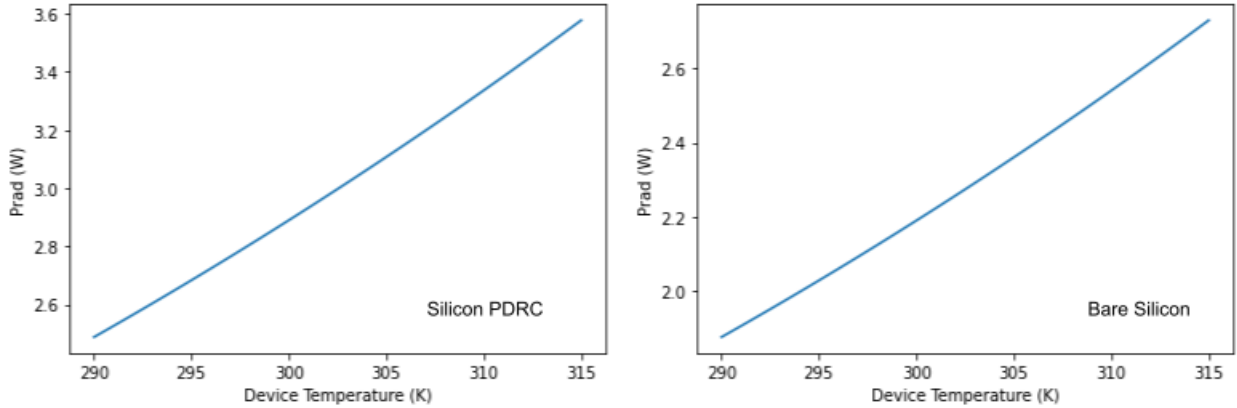


Figure 4.3: Graph of $P_{rad}(T_{dev})$ versus device temperature for the silicon PDRC devices and bare silicon wafer. As temperature falls, so does the rate at which the device converts thermal energy to outgoing radiation.

Figure 4.3 compares the power radiated from the surface of the silicon PDRC device and bare silicon device. Note the power at each temperature is higher for the PDRC device than the bare wafer. This result is attributed to the higher emissivity of the PDMS layer.

Blackbody radiation is emitted at a rate proportional to T^4 consistent with the Stephan-Boltzmann Law in equation ???. Figure 4.4 plots the logarithms of the $P_{rad}(T_{dev})$ with T_{dev} so we can extract the power relationship to confirm that our model agrees with the Stephan-

Boltzmann Law. We find that the slope of the PDRC device is 4.39 while the bare control is 4.50. We expect the slope to be 4, as predicted by the Stephan-Boltzmann Law. This slight discrepancy is likely a result of our calculation using Reimann Sums overstep wise wavelength intervals to approximate the integral of the blackbody curves over the spectrum.

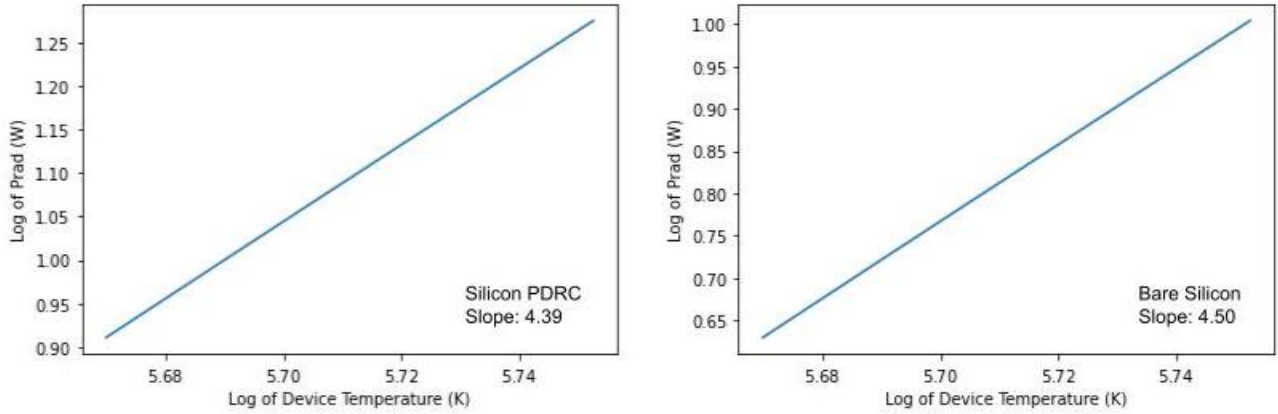


Figure 4.4: Graph of the log base 10 of $P_{rad}(T_{dev})$ and T_{dev} .

4.1.2 Power absorbed from solar radiation: $P_{sun}(\theta_{sun})$

The power absorbed from the sun light, $P_{sun}(\theta_{sun})$, is not dependent on the device temperature or the temperature of the air, as shown in figure 4.5. Rather P_{sun} is a function of (θ_{sun}) , the incident angle of the sun, and can be thought of as scaling the amount radiation that reaches the earth's surface by the device's absorptivity.

It is expected that the bare silicon has a higher $P_{sun}(\theta_{sun})$ than the PDRC device. The bare silicon has lower reflectivity than the PDRC device; more of the solar spectrum is absorbed by the bare silicon than the silicon PDRC device. Hence, we see a higher radiative transfer from the sun.

For the model, we used open sourced NREL reference spectra measured with the sun directly overhead as our input for $I_{AM1.5}(\lambda)$ in equation 4.3. Figure 4.6 plots this data [36]. $P_{sun}(\theta_{sun})$ is calculated normal to the earth's surface so $(\theta_{sun})=0$ in the power balance model.³ The power absorbed by the device for incident sunlight is:

$$P_{sun}(\theta_{sun}) = A \int_0^{\infty} I_{AM1.5}(\lambda) \alpha_{dev}(\theta_{sun}, \lambda) d\lambda \quad (4.3)$$

Notice in Figure 4.6, the AM1.5 spectrum is concentrated in the visible range. By having high reflectivity levels and low absorptivity levels over these shorter wavelengths, the PDRC

³In order for the reference spectra to be compatible with our model, we had to ensure that there was a value for the $I_{AM1.5}(\lambda)$ at each wavelength for the measured absorption values $\alpha_{dev}(\theta_{sun}, \lambda)$. Since our data included smaller steps between wavelengths, the $I_{AM1.5}(\lambda)$ is approximated steps as seen in figure 4.6.

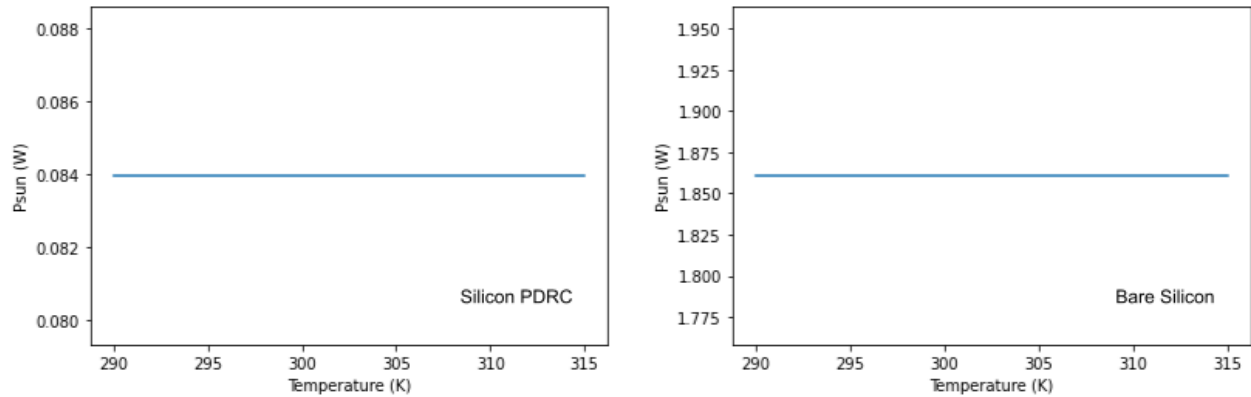


Figure 4.5: Graph of $P_{\text{sun}}(\theta_{\text{sun}})$ versus device temperature T_{dev} for the silicon PDRC device and bare silicon measured at normal incidence ($\theta_{\text{sun}} = 0$). Note there is no temperature dependence.

devices limit the amount of heating due to solar radiation.

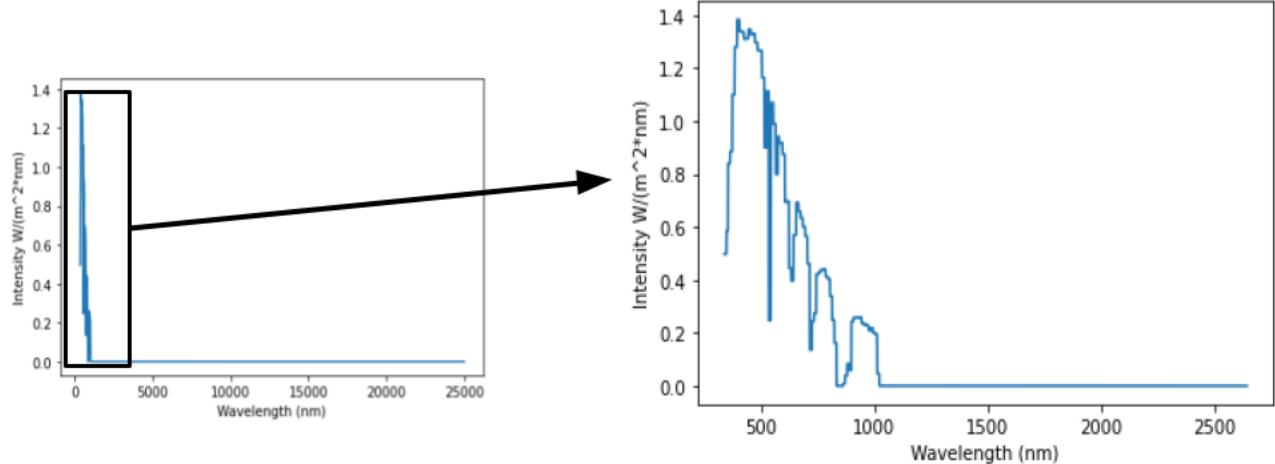


Figure 4.6: The AM1.5 spectrum used in the power balance model extracted from NREL open-source terrestrial solar spectral irradiance data [36].

4.1.3 Power absorbed from thermal radiation by the atmosphere: $P_{atm}(T_{amb})$

The power absorbed by the device from thermal radiation by the atmosphere, $P_{atm}(T_{amb})$, can be qualitatively broken down to the atmosphere's black body emission $I_{bb}(T_{amb}, \lambda)$ scaled by the device absorption $\alpha_{dev}(\theta, \lambda)$ and overall atmospheric emissivity $\epsilon_{atm}(\theta, \lambda)$. In our model, $\epsilon_{atm}(\theta, \lambda) = 0.8$.⁴ A useful discussion of atmospheric thermal radiation, including a rationale for focusing on heat exchange with the troposphere on the ground, can be found in work by Sun et al. [48].

Following the discussions in chapter 2, the power absorbed from atmospheric thermal radiation is:

$$P_{atm}(T_{amb}) = 2\pi A \int_0^{\pi/2} \left[\int_0^{\infty} I_{bb}(T_{amb}, \lambda) \epsilon_{atm}(\theta, \lambda) \alpha_{dev}(\theta, \lambda) d\lambda \right] \sin(\theta) \cos(\theta) d\theta \quad (4.4)$$

$\alpha_{dev}(\theta, \lambda)$ refers to the absorptivity of the device. $P_{atm}(T_{amb})$ is temperature dependent but is dependent on ambient temperature T_{amb} , not the device temperature T_{dev} . As a result, as the device changes its temperature, $P_{atm}(T_{amb})$ will remain constant. Figure 4.7 shows how $P_{atm}(T_{amb})$ changes for various ambient temperatures.

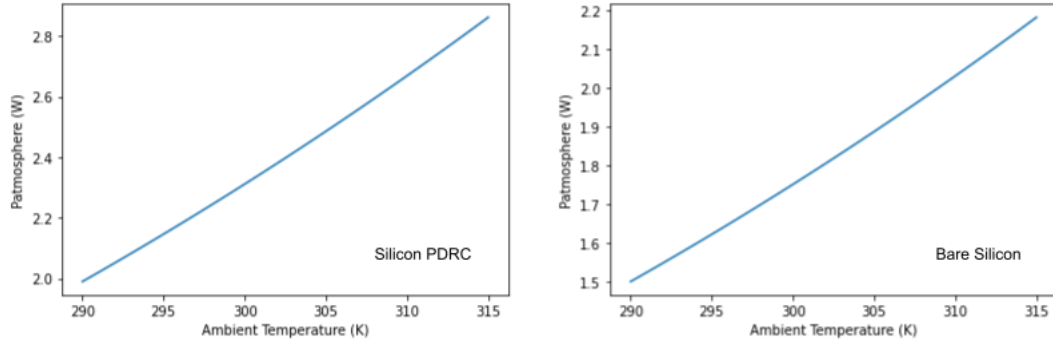


Figure 4.7: This graph shows the relationship between $P_{atm}(T_{amb})$ and ambient temperature for the silicon PDRC device and bare silicon.

Because the PDRC device is designed to be highly emissive at long λ s, absorption of the silicon PDRC device is higher than the bare silicon. Hence, we would expect $P_{atm}(T_{amb})$ to be higher at each temperature for the PDRC device than the bare silicon as shown in figure ??.

⁴The American Chemical Society Climate Science Working Group determined, for a single-layer atmosphere model, atmospheric emissivity is about 0.8 [43].

4.1.4 Power gained from conduction & convection: $P_{cond+conv}(T_{dev}, T_{amb})$

The power gained from conduction convection, $P_{cond+conv}(T_{dev}, T_{amb})$, is dependent on three variables, the ambient temperature T_{amb} , the temperature of the device T_{dev} , and a thermal coefficient, $h_c = 10 \frac{W}{m^2*K}$.⁵

$$P_{cond+conv}(T_{dev}, T_{amb}) = Ah_c(T_{amb} - T_{dev}) \quad (4.5)$$

If we assume ambient temperature to be $T_{amb} = 307K$, we then plot $P_{cond+conv}(T_{dev}, T_{amb})$ against the difference in temperature between ambient and the device. Figure 4.8 shows that $P_{cond+conv}(T_{dev}, T_{amb})$ grows with the difference between T_{dev} and T_{amb} . Hence, as the device temperature falls, $P_{cond+conv}(T_{dev}, T_{amb})$ works to lower the overall cooling capacity of the device, P_{cool} .

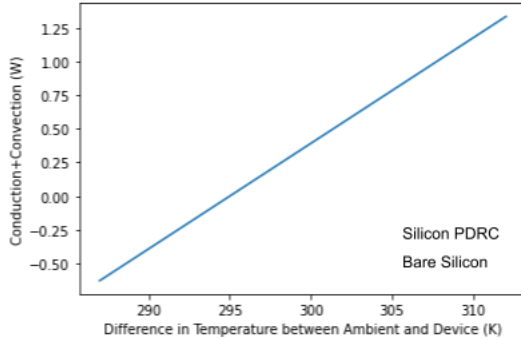


Figure 4.8: Graph of $P_{cond+conv}(T_{dev}, T_{amb})$ against the difference between T_{dev} and T_{amb} for the silicon PDRC device and bare silicon wafer.

These two graphs are the same because we use the same coefficient for the two wafers h_c . Note that $P_{cond+conv}(T_{dev}, T_{amb})$ will be the same for all devices because it does not depend on emissivity $\epsilon_{atm}(\theta, \lambda)$ or absorptivity $\alpha_{dev}(\theta, \lambda)$.

4.1.5 P_{cool}

The above four terms, $P_{rad}(T_{dev})$, $P_{sun}(\theta_{sun})$, $P_{atm}(T_{amb})$, and $P_{cond+conv}(T_{dev}, T_{amb})$ are the determinants of passive daytime radiative coolers cooling capacity.

$$P_{cool} = P_{rad}(T_{dev}) - P_{atm}(T_{amb}) - P_{sun} - P_{cond+conv}(T_{dev}, T_{amb}) \quad (4.6)$$

$P_{rad}(T_{dev})$ falls as the device temperature decreases. $P_{sun}(\theta_{sun})$ and $P_{atm}(T_{amb})$ are not dependent on device temperature. $P_{cond+conv}(T_{dev}, T_{amb})$ depends on the difference between device temperature and ambient temperature. As a result, as the devices fall in temperature,

⁵Previous researchers have measured this value to be $10 \frac{W}{m^2*K}$ [27]. For simplicity, we use the same value here, but we note that in future work h_c should be measured under local conditions.

the overall cooling capacity P_{cool} of the device also falls. Figure 3.3 shows how P_{cool} changes with device temperature for the silicon PDRC device and bare silicon wafer. One feature of figure 3.3 to note is that the bare silicon wafer is negative at the graphed temperatures. Negative P_{cool} values indicate that the silicon wafer is heating up, rather than cooling down as is reflected in the final temperature. When P_{cool} goes to zero, the temperature of the PDRC is 302.5 K while the temperature of the bare silicon is 318.8 K.

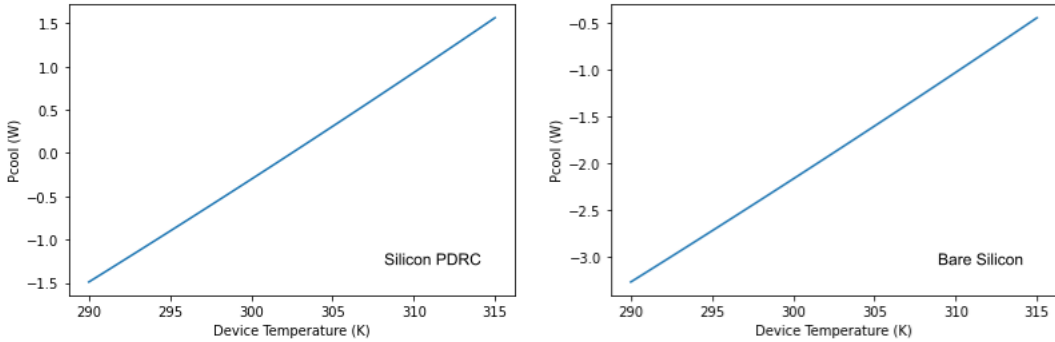


Figure 4.9: Graph of P_{cool} against device temperature for silicon PDRC device and bare silicon. P_{cool} becomes negative at $T_{dev}=302.5$ K for the PDRC silicon device and at $T_{dev}=318.8$ K for the bare silicon.

Given P_{cool} falls with T_{dev} , these devices will not cool down indefinitely. Rather, they will reach an equilibrium state over a certain period of time. The following sections detail how we translate P_{cool} in Watts to a change in device temperature and how we determine the overall time it takes for the device to reach its equilibrium state.

4.1.6 Summary and limitations

This model allows us to examine which radiative sources have the largest impact on the heating and cooling of the PDRC devices by breaking down P_{cool} to each of its components. $P_{atm}(T_{amb})$ is the largest heating source in our model, which confirms the idea that atmospheric gases are a major contributor to earth's surface heating. As more greenhouse gases are added to the atmosphere, $P_{atm}(T_{amb})$ will rise, suppressing the value for P_{cool} .

The power balance model is limited to calculating device cooling power for when the sun is directly overhead due to AM1.5 spectrum data availability. This fixed position model calculates the cooling power at peak solar irradiance at noon, but not at later or earlier times in the day. Hence, the model does not fully represent testing that is conducted over long time periods or at later or earlier periods in the day.

In the results below, we have run the model assuming a value for ambient temperature T_{amb} of 307 K. However, actual testing conditions, particularly in Claremont, CA, can easily reach up to 315K.

4.2 Going from P_{cool} to device temperature

Up until now, discussions of the model have focused on the cooling capacity of the devices in terms of watts, however we are interested in a total device change in temperature. Using the device's specific heat, we can calculate a change in temperature from P_{cool} using the equation 4.8 where P_{cool} is power in watts, m_{device} is the mass of the device, c_{device} is the specific heat of the device, and ΔT_{device} is the change in temperature per second.

$$\begin{aligned} P_{cool} &= m_{dev} * c_{dev} * \Delta T_{modeled} \\ \Delta T_{modeled} &= \frac{P_{pcool}}{m_{dev} * c_{dev}} \end{aligned} \quad (4.7)$$

In order to use this equation, we must first measure the specific heat capacity of the different devices and their controls. Table 3.2 in the methods chapter lists the measured specific heat c_{device} and mass m_{dev} for each device. The power balance equations calculate P_{cool} from each device's emissivity spectrum.

4.2.1 Extracting Steady State Temperature from P_{cool}

When we run through the model and convert the cooling power to a change in device temperature using the specific heat values, our result is the change in temperature at a specific moment, not the overall equilibrium temperature of the device T^* . Therefore, to calculate the devices' overall drop in temperature relative to ambient temperature, the model must iterate through multiple loops to find how the temperature changes over time. Since both $P_{rad}(T_{dev})$ and $P_{cond+conv}(T_{dev}, T_{amb})$ have a dependence on the temperature of the device, we must recalculate each component of the model, accounting for the changing device temperature.

As shown in Figure 4.9, P_{cool} falls with device temperature. In Figure 4.10, the rate of temperature change falls with P_{cool} . Therefore, as the device temperature T_{dev} falls, so does the rate of temperature change. This relationship between the rate of temperature change and T_{dev} is expected. Since P_{cool} is directly proportional to ΔT_{dev} , both variables should have the same relationship with the device temperature.

With this relationship in mind, once P_{cool} reaches zero the system will reach an equilibrium state. Qualitatively this result makes sense. At $P_{cool} = 0$, $P_{rad}(T_{dev})$ balances out with the other radiative sources; in this equilibrium state, there is neither heating nor cooling. Figure ?? shows how the device temperature falls over time if the model is allowed to iterate until $P_{cool} >= 0.00005$, which is taken to be zero, for the silicon PDRC device and bare silicon.

Using the model parameters discussed above, starting at an ambient temperature at 307K, the silicon PDRC device will lower its temperature by 4.52 K to a steady state temperature T^* of 302.5 K. If we use $P_{cool} < 0.00005$ as the criteria for "reach steady state," it takes the device a total of 573 seconds or 9 minutes and 33 seconds to reach this state below ambient. Beginning at the same ambient temperature, the bare silicon wafer heats up to T^* of 318.9K

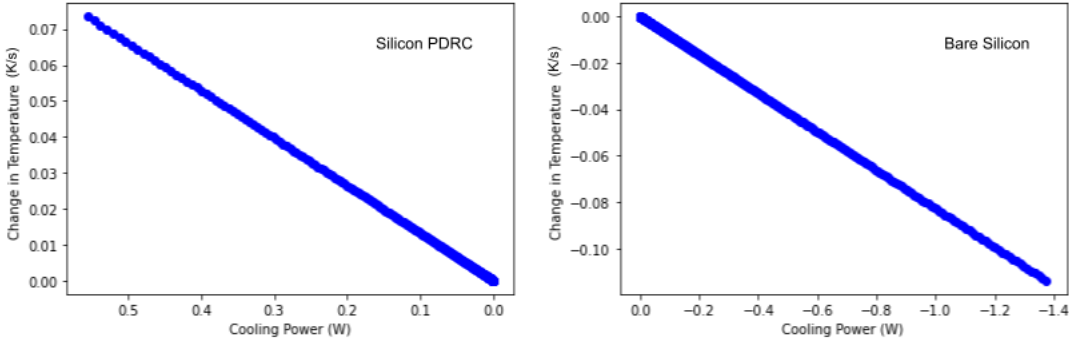


Figure 4.10: Graph of $\Delta T_{device}/\text{second}$ against P_{cool} for the Silicon PDRC device. T_{amb} is assumed to be 307K.

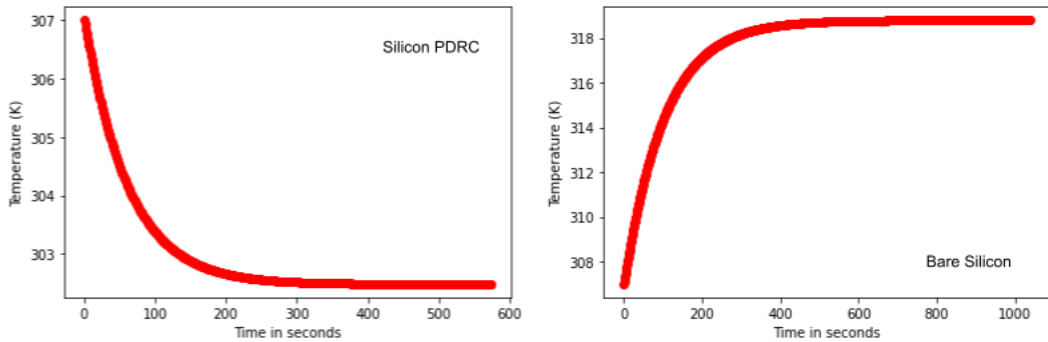


Figure 4.11: Graph of T_{device} against time for the silicon PDRC device and bare silicon wafer

over the course of 17 minutes and 17 seconds. Given bare silicon lacks the reflective layer and emissive layer, it is expected that it would heat, rather than cool, when run through the heat transfer model. The following section details the full results of power balance model.

4.3 Comparing Device Performance

In this section, we compare the predictions of our model to rooftop measurements done by Paul McKinley of the PDRC devices and their controls midday. In the modeling, we have taken the ambient temperature T_{amb} to be 307K. Note that during rooftop testing, T_{amb} can vary from 300 K to 315 K depending on the time of day. $T_{amb} = 307$ K refers to the ambient temperature at noon during the silicon testing trial. Likewise, we assume in the model perfect weather conditions, with no clouds and low humidity, whereas the actual rooftop measurement conditions varied.

The model also includes some simplifications, which includes ignoring the angular de-

pendence of emissivity and an assumed value for the conduction and convection thermal coefficient h_c . Because of these discrepancies, we do not expect to see quantitative agreement between the predicted and measured temperatures. However, we do expect order-of-magnitude agreement between the predicted and measured temperatures and that the general trends (for example, which devices cool the best) will agree.

4.3.1 Silicon PDRC Device

The results of the model for the silicon based PDRC device and controls are shown in Table 4.1. As shown in figure 4.11, the model predicts that the silicon PDRC device cools 4.52°C below ambient. Compared to the predictions for the two controls, the silicon PDRC device cools a total of 5.7°C below the silver-control and a total of 16.3°C below the bare silicon control. These results are expected given that the PDMS layer on the PDRC device is the driver of the sub-ambient cooling. Furthermore, the silver-coated control is more reflective of solar radiation at visible wavelengths than the bare wafer and, therefore, does not absorb as much solar radiation.

These results are in excellent agreement with McKinley's daytime outdoor testing results. While the model consistently predicts absolute temperatures with a 5K offset from outdoor results, McKinley's measured temperature differences are within the model predictions. The model and measurements both show the full PDRC device being 5.5K cooler than the control sample of silicon coated with silver. Similarly, the model predicts a temperature difference of 16.31K between the bare silicon control and silicon PDRC device, while outdoor testing results show a 19.3K. Therefore, in the case of the silicon based device and controls, the model meets both targets: (better than) order-of-magnitude agreement between the predicted and measured temperature, as well as quantitatively consistent trends in the performance of the PDRC device relative to the controls. Table 4.1 details the results from the silicon device testing.

Silicon Devices: $T_{amb} = 307$ K			
Wafer	Model Steady State T^* (K)	Model ΔT (K)	Experimental ΔT_{exp} (K)
Si PDRC	302.5	-4.52	0
Si + Ag	308.2	+1.19	+5.5
Bare Si	318.79	+11.79	+19.3

Table 4.1: This table details the results for the silicon based devices. ΔT is measured in relation to ambient T_{amb} , which is assumed to be $T_{amb} = 307$ K. Each result from the model is then compared to Paul McKinley's rooftop experiments. The column labeled ΔT_{exp} documents the experimental ΔT relative to T_{amb} measured in outdoor testing. .

$$\Delta T = T_{amb} - T_{measured} \quad (4.8)$$

4.3.2 Fused Silica PDRC Device

The results of the model for the fused silica based PDRC device and its controls are shown in Table 4.2. The model predicts that the fused silica PDRC device cools by 4.71°C . It is expected that the fused silica device would be predicted to have a slightly larger drop below ambient than the silicon device given that fused silica is more emissive than silicon in the IR.

The results for the fused silica PDRC device and the silver-coated control sample are in reasonable agreement with McKinley's daytime outdoor testing results. Both the predictions and measurements show that the PDRC devices is several degrees cooler than the silver coated fused silica control.

One unexpected result from the model is that a bare fused silica wafer shows a more significant temperature drop than the PDRC device. Given fused silica is transparent, it is not possible to measure its temperature change on the roof because the sun's rays pass through the device and are absorbed by the thermocouple. Hence, this result cannot be confirmed in outdoor testing due to the transparency of fused silica. Looking at the raw data, average emissivity of the PDRC device is 68% while average emissivity for the bare fused silica is 32%. This result should be further examined as it seems inconsistent.

Note that the fused silica has the silver-coated on the bottom of the device, while PDMS is deposited on top. The silver-coated does experience a 1.0°C rise that is not seen in the outdoor testing results. However, this heating is still significantly lower than the silicon silver-coated control, re-affirming that fused silica is, by itself, highly emissive.

Fused Silica Devices: $T_{amb} = 307 \text{ K}$			
Wafer	$T^* \text{ (K)}$	$\Delta T \text{ (K)}$	$\Delta T_{experimental}$
FS PDRC	302.3	-4.71	-3.5
FS + Ag	307.99	+0.99	-1.3
Bare FS	302.2	-4.80	uncertain

Table 4.2: This table details the results for the fused silica based devices. ΔT is measured in relation to ambient T_{amb} , which is assumed to be $T_{amb} = 307 \text{ K}$. Each result from the model is then compared to Paul McKinley's rooftop experiments. The column labeled ΔT_{exp} documents the experimental ΔT relative to T_{amb} measured in outdoor testing.

4.3.3 Summary of Model Results

We successfully modeled sub-ambient cooling for both the silicon and fused silica PDRC devices. The fused silica and silicon PDRC devices model sub-ambient cooling of 4.7K and 4.5K respectively reaching a temperature of 302.3 K and 302.5 K. The predictions of our model are in excellent agreement with the experimental rooftop testing. For the silicon devices we are able to accurately predict the performance of the PDRC devices relative to

the controls. The fused silica PDRC device is also in good agreement with the outdoor testing result, modeling within a 1.5 K of outdoor testing. The fused silica bare wafer cooled to roughly the same temperature below ambient as the PDRC device.

One possible explanation for the divergence from predicted temperatures and outdoor testing results is our outdoor measurement of ambient. Future outdoor testing will utilize a Stevenson Screen for more precise measurements. However, the outdoor measurements of ambient referenced in this results chapter did not meet the criteria for measuring ambient temperature described in the methods chapter. Another possible cause for divergence is in our use of the thermal coefficient h_c in the $P_{cond+conv}(T_{dev}, T_{amb})$ term.

4.4 Additional Model Tests

This section details additional tests that were performed on the model examining the model's sensitivity to parameters whose values have some uncertainty such as specific heat capacity and emissivity.

4.4.1 Adjusting Specific Heat

Table 4.3 shows the results of the model for three different specific heats using the silicon PDRC device. The equilibrium temperature of the device is determined by the power balance equation. When $T_{dev} = T^*$, $P_{cool}=0$, therefore:

$$P_{rad}(T_{dev}) = P_{atm}(T_{amb}) + P_{sun} + P_{cond+conv}(T_{dev,T_{amb}}) \quad (4.9)$$

This equality is independent of heat capacity. When changing the specific heat in the model, the overall equilibrium temperature of the device does not change. Rather the time it takes to reach equilibrium changes. A higher specific heat means the device requires more energy or power to change the temperature of the device than lower specific heats. Raising the specific heat lowers the temperature step at each iteration at the model. Specific heat, therefore, controls the rate at which the device cools, but not the overall equilibrium temperature. Note here that these trials were run at room temperature, $T_{amb}=294\text{K}$.

Silicon PDRC Devices: $T_{amb} = 294\text{ K}$			
Wafer	Specific Heat C (J/(kg*K))	T^* (K)	Time to T^*
Si PDRC	800	290.2	15 mins, 31 secs
Si PDRC	504	290.2	9 mins, 45 secs
Si PDRC	200	290.2	3 mins, 50 secs

Table 4.3: This table shows how the model output changes by varying C. Equilibrium temperature T^* remains unchanged, while the time it takes to reach steady state does.

4.4.2 Adjusting Emissivity

Table 4.4 shows the results of the model for testing four different emissivity values using the silicon PDRC device. Emissivity $\epsilon_{dev}(\theta, \lambda)$ impacts overall cooling and time to steady state. A higher $\epsilon_{dev}(\theta, \lambda)$ drives more significant cooling because the device is more efficient at transferring heat to its surroundings. For the same reasons, a higher $\epsilon_{dev}(\theta, \lambda)$ also corresponds to lower time to equilibrium. The table below shows the model results for three different runs of the model. For the four different runs, we scaled the measured emissivity spectrum by a factor of 1.05, 1, 0.95, and 0.6. These trials were also run at $T_{amb}=294$.

Silicon PDRC Devices: $T_{amb} = 294$ K			
Wafer	$\epsilon_{dev}(\theta, \lambda)$	ΔT (K)/ T^*	Time to T^*
Si PDRC	$1.05 * \epsilon_{dev}$	-3.92/290.1	9 mins, 36 secs
Si PDRC	ϵ_{dev}	-3.78/290.2	9 mins, 45 secs
Si PDRC	$0.95 * \epsilon_{dev}$	-3.66/290.3	9 mins, 50 secs
Si PDRC	$0.6 * \epsilon_{dev}$	-2.61/291.4	16 mins, 48 secs

Table 4.4: This table shows how the model output changes by varying C. Equilibrium temperature T^* remains unchanged, while the time it takes to reach steady state does.

4.4.3 Conclusions

The criteria set forth for a passive daytime radiative cooler discuss the device's spectral properties, not the material's specific heat capacity. These results re-affirm that choice. While a lower specific heat capacity does lead to more rapid cooling, it has no impact on the overall cooling ability of the PDRC device. The spectral properties of the devices such as emissivity, rather, are the driving factors. Cooling speed is not a factor to overlook entirely. Faster cooling methods will be more attractive when it comes to real world applications of these devices.

Chapter 5

Conclusions

By mid century, the National Climate Assessment estimates that there will be 20-30 more days over 90 degrees Fahrenheit in most areas in the US [22]. To help people cope with these rising temperatures, the global demand for air conditioning is expected to triple by 2050, bringing with it a massive surge in energy demand and carbon emissions [26]. Therefore, moving forward, there needs to be significant shifts in our cooling technology to avoid excess deaths and a positive feedback loop in which increased demand for cooling leads to a further rise in global temperatures. Passive Daytime Radiative Cooling devices are a potential part of the solution to this cooling crisis. PDRC devices require no electricity to lower a surface's temperature and are relatively low cost, particularly once you factor in the long-term savings from reduced electricity usage.

5.0.1 Our Work

While previous experimental work with these technologies has focused on outdoor sub-ambient cooling performance, few papers have examined the power balance model to this depth. Modeling how PDRC devices function by breaking down the individual components that lead to device cooling allows us to understand the characteristics that contribute to cooling and better maximize performance for current and future device structures.

Our model aims to predict the behavior of the PDRC devices in outdoor testing conditions. Overall, this goal was achieved. When comparing the predicted performance of the silicon and fused silica devices to their respective controls, the predictions mirrored outdoor testing results exceptionally well. The model predicted the silicon PDRC device would have an equilibrium temperature 5.7 K below that of the silver-coated control, whereas outdoor results observed a 5.5 K temperature difference. Similarly, the model predicted that the PDRC device would equilibrate 16.3 K below the bare silicon control, while outdoor testing observed a 19.3 K drop. For the fused silica PDRC device, the model predicted a cooling of 4.7K while outdoor testing results saw 3.5 K of cooling. Therefore, the model is in great agreement with the outdoor experiment by quantitatively predicting temperatures differences between devices, controls ambient for the silicon device, and for the overall

sub-ambient cooling of the fused silica device.

While these similarities with outdoor testing show that our model is capable of high level predictions, there are factors that may contribute to such discrepancies as modeling 4.52K of cooling for the silicon PDRC device that was not observed on the roof. The model assumes perfect weather conditions, low humidity and zero cloud cover. However, these are not the given outdoor conditions. The model is also currently limited to calculating device cooling power for when the sun is directly overhead, at peak solar irradiance because we have not measured $\epsilon(\lambda)$ as a function of angle. In comparison, outdoor testing occurs over the length of four to five hours, allowing the sun to move positions in the sky. The model also assumes values for h_c and ϵ_{atm} , which should be measured under local conditions.

5.0.2 Future Directions

The power balance model successfully predicts the behavior of the PDRC devices in outdoor testing. Future work can improve upon the model parameters and outdoor testing results.

Power Balance Model

Currently the model uses a literature value for the thermal coefficient h_c in the $P_{cond+conv}(T_{dev}, T_{amb})$. However, if we can experimentally measure a value for h_c , then our model will be able to better reflect our local outdoor testing climate. The other major assumption that this model makes is the value for T_{amb} . Currently the model uses a value of $T_{amb} = 307$ K, which is the ambient temperature at noon during the silicon outdoor testing trial. However, in real outdoor conditions, the value of ambient temperature changes over the course of the testing period. We can improve the overall accuracy of the model's predictions if we adjust the code to reflect a changing ambient temperature.¹

Additionally, we have yet to explore how the model predicts the behavior of PDRC devices in nighttime conditions. However, the model parameters do allow for this type of analysis. By setting $P_{sun}=0$, we can mimic nighttime testing conditions. Future work should explore this side of the model.

Outdoor Testing

Part of the work for this thesis included improving upon the experimental setup designed by Paul McKinley. These upgrades included improving upon the resolution of the temperature probes and data logger. We also designed and constructed a Stevenson Screen to improve the overall accuracy of the ambient probe measurement. However, we do not have a complete set of results using these new upgrades. Therefore, in this thesis, model predictions were compared to Paul McKinley's outdoor testing results. Future rooftop testing will utilize these adjustments, which improve the model and rooftop comparisons.

¹The current outdoor testing has yet to utilize the new Stevenson Screen, which will improve the overall accuracy of our outdoor measurement of ambient.

Device Applications

The silicon and fused silica based devices are the two PDRC devices currently tested in the lab. However, variations of these devices could prove interesting. For instance, one application of PDRC technologies is in architecture. Given PDMS is highly emissive, it could be worthwhile examining how PDMS deposited on various roofing materials coated in a matted seal impacted the material's temperature. Another idea is to explore the applications of fused silica as transparent and emissive material. A device that has two fused silica wafer substrates separated by a layer of PDMS is still transparent and therefore has applications to passive daytime radiative cooling windows.

5.0.3 Final Remarks

Our model and outdoor testing reflects around 3-5K of sub-ambient cooling. While these results may not appear to reflect major sub-ambient temperature changes, a few degrees can have a significant impact on one's living environment. Currently, this model is a powerful tool to understand what device parameters are most important to optimize in future designs so that we can achieve a more significant level of cooling. Looking forward, incorporating PDRC technologies into building and urban design can help reduce the overall demand for cooling. By lowering electricity load, PDRC technologies can help make cooling more reliable, accessible, and affordable.

Appendix A

An appendix

A.1 Nicolet is50 FTIR Spectrometer Procedure

NOTE: The chemistry department requires all users of the Nicolet is50 FTIR Spectrometer to have signed the “Commitment to Safety in the Laboratory” form and wearing the proper dress code as defined in the form guidelines (closed toed shoes, long pants, long sleeve shirts, lab coat, safety goggles, protective gloves, hair tied back).

Safety Information

“High Voltage Hazard – This instrument operates at potentially lethal voltages. Do not open any panels or attempt to service the instrument. Report any leaks or damaged cables immediately.” “Laser Hazard – This instrument utilizes a Class 2 laser. Keep eyes and reflective items away from the sample compartment.”

Switching out the Module for the 10Spec

1. The FTIR should be on by default. If it is off, there is an on switch in the rear left. modules can be swapped with the machine on and will prompt a change to the experiment file when properly installed.
2. If there is a hood on the FTIR machine, open it. Turn the knob to the left, and lift the hood vertically upwards. There is a notch in the rear of the hood.
3. Remove the base plate, lift it carefully up vertically until it clears the machine and place it off to the side of the machine.
4. Open up the black briefcase and find the base plate, which looks very similar to the base plate that was just removed. Place the baseplate on the FTIR machine, lining up the front and back holes to pins so the plate is secure.

5. Place the box on the baseplate. There are two notches on the bottom of the box that align with the baseplate. Very very careful not to touch the lens or bump the box on the sides of the FTIR.

Collecting Reflection Data

1. Start the “OMNIC” software from the desktop.
2. Place the mask, flat side up. Then using gloves place the gold plate gold side down on the mask by carefully only touching the sides.
3. Hit col bkg to collect a background measurement of the gold plate.
4. Using gloves again carefully switch out the gold plate with your sample
5. Hit the Col Smp, to take your measurement. Hitting add to window will layer your results on the graph. Repeat step 11 as necessary for additional samples.

Switching out the Module for the transmission measurements

- Follow the same procedure for switching out the module to switch in the transmission module.

A.2 Data logger Manual

<https://www.reedinstuments.com/pdfs/cache/www.reedinstuments.com/r2450sd/manual/r2450sd-manual.pdf>

Bibliography

- [1] REED R2450SD Data Logging Thermometer.
- [2] SkyCool Radiative Cooling Panels: Solving the World's Cooling Challenge.
- [3] Washington post., Air conditioning has a climate problem. New technology could help.
- [4] Climate and Earth's Energy Budget, Jan. 2009. Publisher: NASA Earth Observatory.
- [5] 4. Radiant Power Density, Nov. 2018.
- [6] Calculating Planetary Energy Balance & Temperature | UCAR Center for Science Education, June 2021.
- [7] Methane emissions are driving climate change. Here's how to reduce them., Aug. 2021. Section: News and Stories.
- [8] How Do You Measure Air Temperature Accurately? *NIST* (Feb. 2022). Last Modified: 2022-04-13T15:12-04:00.
- [9] AERONAUTICS, N., AND ADMINISTRATION, S. Climate Science Investigations South Florida - Energy: The Driver of Climate, 2023.
- [10] (AMS), A. M. S. Radiation frost - Glossary of Meteorology.
- [11] ASTRONOMY, E. R. Chapter 2 Radiation Fundamentals.
- [12] BHATIA, B., LEROY, A., SHEN, Y., ZHAO, L., GIANELLO, M., LI, D., GU, T., HU, J., SOLJAČIĆ, M., AND WANG, E. N. Passive directional sub-ambient daytime radiative cooling. *Nature Communications* 9, 1 (Nov. 2018), 5001. Number: 1 Publisher: Nature Publishing Group.
- [13] CAROSEN A MEOLA, SIMONE BOCCARDI, G. M. C. Chapter 3 - Infrared Thermography Basics. In *Infrared Thermography in the Evaluation of Aerospace Composite Materials*, C. Meola, S. Boccardi, and G. m. Carlomagno, Eds. Woodhead Publishing, Jan. 2017, pp. 57–83.

- [14] CATALANOTTI, S., CUOMO, V., PIRO, G., RUGGI, D., SILVESTRINI, V., AND TROISE, G. The radiative cooling of selective surfaces. *Solar Energy* 17, 2 (May 1975), 83–89.
- [15] CHEN, M., PANG, D., CHEN, X., YAN, H., AND YANG, Y. Passive daytime radiative cooling: Fundamentals, material designs, and applications. *EcoMat* 4, 1 (2022), e12153. eprint: <https://onlinelibrary.wiley.com/doi/pdf/10.1002/eom2.12153>.
- [16] CLIMATE, AND COALITION, C. A. Tropospheric ozone.
- [17] DEPARTMENT OF ENERGY, S. E. T. O. Solar Radiation Basics.
- [18] EISBERG, R., AND RESNICK, R. *Quantum Physics of Atoms, Molecules, Solids, Nuclei, and Particles*., 2nd edition ed. Hamilton Printing Company, 1985.
- [19] ENVIRONMENTAL, F. Solar Radiation & Photosynthetically Active Radiation, 2014.
- [20] EPA. Keeping your cool: How communities can reduce the heat island effect.
- [21] EVANS, P. Specific heat capacity of materials, Oct. 2016.
- [22] FOR CLIMATE, C., AND SOLUTIONS, E. Heat Waves and Climate Change.
- [23] GENTLE, S. Radiative Heat Pumping from the Earth Using Surface Phonon Resonant Nanoparticles, 2007.
- [24] GRANT W. PETTY. *A First Course in Atmospheric Radiation*, second edition ed. Sundog Publishing, 2006.
- [25] HABY, J. The Cooling Effects of Surface Snow Cover.
- [26] (IEA), I. E. A. The Future of Cooling – Analysis, 2018.
- [27] KOU, J.-L., JURADO, Z., CHEN, Z., FAN, S., AND MINNICH, A. J. Daytime Radiative Cooling Using Near-Black Infrared Emitters. *ACS Photonics* 4, 3 (Mar. 2017), 626–630. Publisher: American Chemical Society.
- [28] LAB 2, P. . Heat engines and the peltier device physics 42 lab handout.
- [29] LABORATORY, NASA'S JET PROPULSION, S. U. H. I. o. E. C. A. A. F.-P. S. B. A. B. The Atmosphere: Getting a Handle on Carbon Dioxide.
- [30] LEAH BURROWS YEAR = 2022 URL = <HTTPS://WWW.SEAS.HARVARD.EDU/NEWS/2022/07/HOTTEST-WORLD-AIR-CONDITIONING-ISNT-LUXURY-ITS-LIFESAVER>, URLDATE = 2022-11-07, A. . H. In a hotter world, air conditioning isn't a luxury, it's a lifesaver.

- [31] LI, T., ZHAI, Y., HE, S., GAN, W., WEI, Z., HEIDARINEJAD, M., DALGO, D., MI, R., ZHAO, X., SONG, J., DAI, J., CHEN, C., AILI, A., VELLORE, A., MARTINI, A., YANG, R., SREBRIC, J., YIN, X., AND HU, L. A radiative cooling structural material. *Science* 364, 6442 (May 2019), 760–763. Publisher: American Association for the Advancement of Science.
- [32] LIN, K., DU, Y., CHEN, S., CHAO, L., HIM LEE, H., CHUNG HO, T., ZHU, Y., ZENG, Y., PAN, A., AND YAN TSO, C. Nanoparticle-polymer hybrid dual-layer coating with broadband solar reflection for high-performance daytime passive radiative cooling. *Energy and Buildings* 276 (Dec. 2022), 112507.
- [33] M. BRUNETTI AND F. PRODI. The climate system. *EDP Sciences - SIF* 98 (2015).
- [34] MAGAZINE, ANTHROPOCENE, E. U. How to Prevent Air Conditioners from Heating the Planet.
- [35] MANDAL, J., YANG, Y., YU, N., AND RAMAN, A. P. Paints as a Scalable and Effective Radiative Cooling Technology for Buildings. *Joule* 4, 7 (July 2020), 1350–1356.
- [36] NREL. Reference Air Mass 1.5 Spectra.
- [37] NREL. News Release: Scientists Show Large Impact of Controlling Humidity on Greenhouse Gas Emissions, 2022.
- [38] OSORIO, M., SALAZAR, A., PRIETO, F., BOULANGER, P., AND FIGUEROA, P.
- [39] PRATER, ZEKE HAUSFATHER AND TOM, R. M. Mapped: How ‘proxy’ data reveals the climate of the Earth’s distant past.
- [40] RAMAN, A. P., ANOMA, M. A., ZHU, L., REPHAEILI, E., AND FAN, S. Passive radiative cooling below ambient air temperature under direct sunlight. *Nature* 515, 7528 (Nov. 2014), 540–544. Number: 7528 Publisher: Nature Publishing Group.
- [41] RUSSELL, R. Solar Energy in Earth’s Atmosphere - Windows to the Universe, 2010.
- [42] SHARAYANAN. English: Small solid angle definition, vector version.
- [43] SOCIETY, A. C. A Single-Layer Atmosphere Model.
- [44] TROMBE, F. PERSPECTIVES SUR L’UTILISATION DES RAYONNEMENTS SOLAIRES ET TERRESTRES DANS CERTAINES REGIONS DU MONDE. *PERSPECTIVES SUR L’UTILISATION DES RAYONNEMENTS SOLAIRES ET TERRESTRES DANS CERTAINES REGIONS DU MONDE* (1975).
- [45] US EPA, O. Climate Change Indicators: Climate Forcing, June 2016.

- [46] YANG, Y., AND ZHANG, Y. Passive daytime radiative cooling: Principle, application, and economic analysis. *MRS Energy & Sustainability* 7, 1 (June 2020), 18.
- [47] ZENG, S., PIAN, S., SU, M., WANG, Z., WU, M., LIU, X., CHEN, M., XIANG, Y., WU, J., ZHANG, M., CEN, Q., TANG, Y., ZHOU, X., HUANG, Z., WANG, R., TUNUHE, A., SUN, X., XIA, Z., TIAN, M., CHEN, M., MA, X., YANG, L., ZHOU, J., ZHOU, H., YANG, Q., LI, X., MA, Y., AND TAO, G. Hierarchical-morphology metafabric for scalable passive daytime radiative cooling. *Science* 373, 6555 (Aug. 2021), 692–696. Publisher: American Association for the Advancement of Science.
- [48] ZHAO, D., AILI, A., ZHAI, Y., XU, S., TAN, G., YIN, X., AND YANG, R. Radiative sky cooling: Fundamental principles, materials, and applications. *Applied Physics Reviews* 6 (June 2019), 021306.
- [49] ZHOU, L., SONG, H., LIANG, J., SINGER, M., ZHOU, M., STEGENBURGS, E., ZHANG, N., XU, C., NG, T., YU, Z., OOI, B., AND GAN, Q. A polydimethylsiloxane-coated metal structure for all-day radiative cooling. *Nature Sustainability* 2, 8 (Aug. 2019), 718–724. Number: 8 Publisher: Nature Publishing Group.